

Cell size and actin architecture determine force generation in optogenetically activated cells

T. Andersen,¹ D. Wörthmüller,^{2,3} D. Probst,^{2,3} I. Wang,¹ P. Moreau,¹ V. Fitzpatrick,¹ T. Boudou,¹ U. S. Schwarz,^{2,3,*} and M. Balland^{1,*}

¹Université Grenoble Alpes, CNRS, LIPhy, F-38000 Grenoble, France; ²Institute for Theoretical Physics, Heidelberg University, Heidelberg, Germany; and ³BioQuant-Center for Quantitative Biology, Heidelberg University, Heidelberg, Germany

ABSTRACT Adherent cells use actomyosin contractility to generate mechanical force and to sense the physical properties of their environment, with dramatic consequences for migration, division, differentiation, and fate. However, the organization of the actomyosin system within cells is highly variable, with its assembly and function being controlled by small GTPases from the Rho family. To understand better how activation of these regulators translates into cell-scale force generation in the context of different physical environments, here we combine recent advances in non-neuronal optogenetics with micropatterning and traction force microscopy on soft elastic substrates. We find that, after whole-cell RhoA activation by the CRY2/CIBN optogenetic system with a short pulse of 100 ms, single cells contract on a minute timescale in proportion to their original traction force, before returning to their original tension setpoint with near perfect precision, on a longer timescale of several minutes. To decouple the biochemical and mechanical elements of this response, we introduce a mathematical model that is parameterized by fits to the dynamics of the substrate deformation energy. We find that the RhoA response builds up quickly on a timescale of 20 s, but decays slowly on a timescale of 50 s. The larger the cells and the more polarized their actin cytoskeleton, the more substrate deformation energy is generated. RhoA activation starts to saturate if optogenetic pulse length exceeds 50 ms, revealing the intrinsic limits of biochemical activation. Together our results suggest that adherent cells establish tensional homeostasis by the RhoA system, but that the setpoint and the dynamics around it are strongly determined by cell size and the architecture of the actin cytoskeleton, which both are controlled by the extracellular environment.

SIGNIFICANCE Our work addresses the long-standing question how single cells achieve tensional homeostasis. Tensional homeostasis is a concept derived from the homeostasis principle formulated by Claude Bernard (French physiologist, 19th century), which refers to the ability of organs, tissues, and cells to respond to external disturbances by maintaining a setpoint of mechanical stress. A large body of experimental observations in the field of mechanobiology suggests that cells do adapt to their mechanical environment mainly by keeping their tension constant. We found that cell traction forces return to baseline with near-perfect precision after a transient perturbation in their control structure for force generation, thus validating the concept of tensional homeostasis.

INTRODUCTION

Actomyosin contractility has emerged as a central element of cellular decision-making processes. By actively contracting their environment, cells can sense its mechanical and geometrical properties, with dramatic consequences for

migration, differentiation, and development (1,2). The actomyosin system can be locally organized into fundamentally different architectures. While the actomyosin cortex provides a basic level of contractility at the cellular level, more localized actin structures such as lamellipodia, filopodia, lamella, or stress fibers are assembled dynamically in response to signals that can originate both from outside or inside of cells (3–5). Small GTPases from the Rho family have evolved to spatially and temporally control this large variety of possible actin architectures. These key signaling molecules are activated at membranes and control the assembly and activity of the actomyosin system (6,7). The three most prominent members are Cdc42, Rac1, and

Submitted June 22, 2022, and accepted for publication January 9, 2023.

*Correspondence: schwarz@thphys.uni-heidelberg.de or martial.balland@univ-grenoble-alpes.fr.

T. Andersen, D. Probst, and D. Wörthmüller contributed equally to this work.

Editor: Paul Janmey

<https://doi.org/10.1016/j.bpj.2023.01.011>

© 2023 Biophysical Society.

This is an open access article under the CC BY license (<http://creativecommons.org/licenses/by/4.0/>).



RhoA. Both Cdc42 and Rac1 lead to polymerization of actin at the leading edge through activation of the Arp2/3 complex, but Cdc42 is typically more localized to the very front of a polarized cell, while Rac1 has a broader distribution behind the advancing front of a migrating cell; this agrees with their putative function to mainly control directionality and speed, respectively (8). In marked contrast, RhoA mainly effects contraction based on the assembly and activation of non-muscle myosin II minifilaments (9). This is achieved mainly by simultaneously effecting the phosphorylation of the myosin II regulatory light chain through Rho-associated kinase and polymerization of parallel actin filaments through the formin mDia1. During cell migration, RhoA activity is thought to be localized more to the rear of the cell, to ensure retraction of the trailing edge; but, in practice, its activity has been found to be spatially distributed (10). In particular, it is also an important feature of the lamellum, the region behind the lamellipodium where actomyosin contractility plays an important role for retrograde flow and in which different types of stress fibers form (11). Together, the biochemical regulators from the Rho family ensure that cells can dynamically organize their actomyosin cytoskeleton in response to a large variety of different signals.

On the cellular scale, the main output of the actomyosin machinery of cells is the generation of contractile force that is applied to the physical environment. Starting with the first quantitative measurements of cellular traction forces on soft elastic substrates (12–14), it has been realized that typical cell stresses are in the kPa range and thus match the elastic stiffness of their physiological environment (1,15). In fact one can argue that, in a physiological context, cells have to balance their forces against the environment such that tissue integrity is ensured (16,17). For cell-populated collagen gels, it has been found that cells dynamically counteracted the effect of externally applied or relaxed stress, effectively working toward a setpoint of tension, leading to the concept of tensional homeostasis (18,19). Although this tissue-level response must translate into corresponding behavior of single cells, it is currently unclear if tensional homeostasis in the strict sense also exists at the single-cell level. Combining micropatterning with an AFM setup to dynamically measure and control forces, it has been shown that single-cell tension evolves toward a plateau, but that this setpoint is variable and depends on the loading history (20). In a study using stretchable micropost arrays, it was shown that cells returned to relatively well-defined tension levels within a 30 min adaptation time, and that the regulation of this process was strongly connected to the dynamics of focal adhesions (21). Recent studies using cell stretching by a 3D-printed scaffold demonstrated perfect tensional homeostasis (22), which, however, is perturbed in different ways in mutants that lack one of the three non-muscle myosin II isoforms (23). These experiments show that single cells indeed use

regulatory processes to control their tension levels. Dysregulation of these homeostatic processes is closely related to different types of diseases. In particular, changes in RhoA regulation have been connected to the progression of cancer (24,25). However, it has not been shown yet if the RhoA system itself establishes homeostasis, on which timescales this response works, and how the biochemical network works together with the downstream and more physical processes of force generation.

To address these important questions, here we use non-neuronal optogenetics, which recently has emerged as a promising new method to interrogate cell function with minimal invasion. This technique allows rapid light-mediated protein activation, with the added advantages of low toxicity and reversibility (26,27). Although originally developed for neuroscience, where ion channels or ion transporters are activated by light, during recent years optogenetics has been also increasingly applied to the cytoskeleton, where light-sensitive domains are used to effect an allosteric change in a protein of interest (26,28–30). In particular, non-neuronal optogenetics for the Rho system has been used to control single-cell contractility, using either the CRY2/CIBN-construct (31,32) or the LOV2-construct (33,34). Optogenetic activation of Rho has also been used to reveal mechanical adaptation responses in epithelial cell junctions (35,36), the feedback loops that structure the Rho responses in cells (37) and even cell migration (38).

Here we combine Rho optogenetics with micropatterning and traction force microscopy on soft elastic substrates to measure the input-output relation between biochemical activation and force generation, and to investigate its relation with cell size and actin organization. To disentangle the roles of biochemistry and mechanics for the dynamic cell response, we use mathematical modeling building on an established continuum model for force generation on elastic substrates. We find that the cells perform near-perfect tensional homeostasis after transient optogenetic activation and that the setpoint of their tension depends on cell size and the pre-established actin cytoskeleton organization. We further show that the dynamics toward this setpoint is shaped by fast, asymmetric, and saturable biochemical activation and smoothed by persistence in the force-generating actomyosin machinery.

MATERIALS AND METHODS

TFM gel preparation

Description of the procedure following published work (39). A photomask (TOPAN, Round Rock, Texas, USA), previously rinsed with water and isopropanol, and a glass coverslip (20 mm) are activated together with air plasma (4 min) and oxygen plasma (40 s). Then a pLL-PEG drop (35 μ L) is sandwiched between the chrome side of the mask and the glass coverslip. After 30 min incubation, the glass coverslip is removed and

saved for the following step as it is now a passivated surface. The photo-mask is exposed to deep UV during 3 min from the quartz side, burning the pLL-PEG at defined loci with minimum loss of resolution due to diffraction. Then again, a drop (35 μ L) of sodium bicarbonate (100 mM) solution of fibronectin (20 μ g/mL, Sigma, St. Louis, Missouri, USA) and Alexa546-conjugated fibrinogen (5 μ g/mL, Invitrogen, Carlsbad, USA) is sandwiched between the mask and the passivated glass coverslip and incubated for 30 min. For 4.47 kPa hydrogels, a solution containing 12.5% acrylamide (from 40% stock solution) and 7.5% bisacrylamide (from 2% stock solution) was prepared in a 10 mM DPBS solution (pH 7.4). Finally, the polyacrylamide solution is mixed with passivated fluorescent beads (0.2 μ m, Invitrogen) by sonication before addition of ammonium persulfate and N,N,N',N'-tetramethylmethylenediamine. A drop (47 μ L) of this solution is sandwiched between the patterned region of the mask and a silanized glass coverslip. After 30 min polymerization, the coverslip with the hydrogel is carefully removed from the mask and stored in DPBS solution at 4°C. Cells were plated on them the following day.

Cell culture and plating

Stable cell line NIH 3T3 fibroblasts with CIBN-GFP-CAAX and opto-GEF-RhoA constructs (kindly provided by L. Valon and M. Coppey, Institute Curie, Paris, France) were cultured in Dulbecco's modified essential medium (DMEM) containing 10% fetal bovine serum (FBS) and 0.2% penicillin-streptomycin. Cells were grown in a humidified 5% CO₂ incubator at 37°C. Cells were seeded on patterned substrates at a density of 10,000 cells/cm². All traction force measurements or immunostainings were performed 4 h after seeding to ensure full spreading of the cells. Leibovitz's L-15 medium, supplemented with 10% FBS and 0.2% penicillin-streptomycin, was used as imaging medium for every live imaging experiment.

Live cell imaging and activation

Cell imaging and activation intended for posterior force measurements was carried out using a Nikon Ti-E microscope, Zyla sCMOS camera (Andor, Belfast, UK), and a Plan Apo VC 60 \times /1.40 Oil objective (Nikon, Tokio, Japan). The microscope was equipped with an incubator that maintains the temperature at 37°C. Global cellular photoactivation was performed using a LED light source (X-Cite/XLED1, Lumen Dynamics, Canada) coupled to a Mosaic digital micromirror device (Andor). Depending on the experiment done, activation pulses were 10-20-50-100-150-200 ms long using an LED at 460 nm with a power of 256.7 μ W (measured at the back focal plane of the objective). For our Apo VC 60 \times Nikon NA 1.4 objective, the transmission coefficient at 450 nm is 74% (data from Nikon). From this we deduce the energy sent to the cells by dividing the intensity transmitted by the objective by the surface of the digital micromirror device (DMD). The physical size of our DMD is 854 \times 480 pixels for our 60 \times objective and this gives us an irradiance of 52.7 mW/mm². This finally gives the following energy per pulse sent to the cells of 0.527, 1.054, 2635, 5270, 7905, and 10,540 mJ/mm² for each pulse of 10, 20, 50, 100, 150, and 200 ms, respectively.

Cell stainings

For stress fiber labeling, cells were permeabilized and fixed for 10 min with 0.2% w/v Triton X-100 and 4% paraformaldehyde in DPBS buffer to preserve cell shape. Fixed samples were washed with PBS and incubated in blocking buffer for 45 min. Afterward, cells were stained with phalloidin at 1 mM (Sigma-Aldrich, St. Louis, Missouri, USA) for 1 h and finally mounted on glass slides with Mowiol 4-88 (Polysciences, Warrington, Pennsylvania, USA) and kept at 4°C overnight.

For live actin measurements, cells were incubated overnight in DMEM medium supplemented with 100 nM SiR-actin (SPIROCHROME, Stein am Rhein, Switzerland) and 10 μ M verapamil. Vinculin staining: after 4 h of culture on the micropatterns, cells were fixed with 3.7% formaldehyde in PBS, permeabilized with 0.2% Triton X-100 in TBS (50 mM Tris-HCl, 0.15 M NaCl [pH 7.4]) and blocked with 2% BSA (Sigma-Aldrich) in TBS. The samples were then incubated with primary antibodies against vinculin (Sigma-Aldrich) and detected with Alexa 488-conjugated, isotype-specific, anti-IgG antibodies (Invitrogen). Actin was labeled with phalloidin-TRITC (Sigma) and nuclei were stained with DAPI (Life Technologies, Waltham, Massachusetts, USA). Focal adhesions were quantified by thresholding vinculin images before measuring the resulting total area of focal adhesions using a home-made ImageJ (National Institutes of Health) routine. Both live and fixed actin imaging was carried out with a Leica, Wetzlar, Germany TCS SPE confocal microscope with an HCX PL APO 63 \times /1.40 oil objective. The microscope was controlled through the Leica Application Suite (LAS) X software. Pictures were then processed using Fiji software.

Actin order parameter analysis

This analysis was performed with the ImageJ (National Institutes of Health) plugin OrientationJ, which calculates the local orientation in actin images using the structure tensor (40). The program first smooths the original image using a Gaussian filter. Then, based on the intensity level, the region in the cell is segmented. For each pixel in the cell, the structure tensor J (which has three elements: J_{11} , J_{12} , and J_{22}) is computed in a local neighborhood that is also Gaussian. The orientation angle, the coherency, and a measure of local gradient (gray level is constant or it changes) are computed from the elements of the structure tensor (λ_i are the eigenvalues of J):

$$\begin{aligned} \tan(2\theta) &= \frac{2J_{12}}{J_{22} - J_{11}} \\ \text{coherency} &= \frac{\sqrt{(J_{22} - J_{11})^2 + 4J_{12}^2}}{J_{11} + J_{22}} = \frac{\lambda_1 - \lambda_2}{\lambda_1 + \lambda_2} \\ \text{gradient} &= J_{11} + J_{22} = \lambda_1 + \lambda_2. \end{aligned}$$

The average orientation and order parameter S will be computed by averaging over all pixels for which the coherency is above a threshold value, which can be changed. Average angle is $\theta_m = \langle \theta \rangle_{c>\text{thres}}$ and the order parameter is $S = \langle \cos(2(\theta - \theta_m)) \rangle_{c>\text{thres}}$. S = 1 means that the local orientation is parallel to the average orientation, S = 0 means that they are orthogonal.

Traction force microscopy

Displacement fields describing the deformation of the polyacrylamide substrate are determined from the analysis of fluorescent bead images before and after removal of the adhering cells with trypsin treatment. The displacement field can be obtained by merging the images of the gel under stress, which means while the cell is adherent, and the non-stressed image, which is after the cell has been detached using trypsin. Its calculation is made by a two-step method consisting of particle image velocimetry followed by individual bead tracking (41,42). Force reconstruction was conducted with the assumption that the substrate is a linear elastic half-space, using Fourier transform traction cytometry with zeroth-order regularization (41). The shear modulus of the gels used in these experiments was 5 kPa, as described by (43). All calculations and image processing were performed in

MATLAB combining particle image velocimetry and single-particle tracking.

Statistical analysis

All data were statistically analyzed in GraphPad Prism (GraphPad Software, San Diego, CA, USA). To test the significance in between data, we performed both two-tailed Student's *t*-tests in the case of two data sets and non-parametric Kruskal-Wallis test in the case of three data sets. Error bars on graphs represent the standard deviation.

Mathematical model

Following earlier work on modeling traction forces as a function of cell geometry (44–51), we describe the cell as a thin contractile layer that adheres to an elastic foundation (Fig. 2 *a*). The stress state of the cell layer is given by $\sigma_{ij} = \sigma_{ij,p} + \sigma_{ij,m}$. Here, $\sigma_{ij,p}$ represents the passively generated stresses due to deformation of the cell, while $\sigma_{ij,m}$ accounts for an active stress generated by actomyosin contraction. The motor stress is again divided into a constant background stress $\sigma_{ij,bck}$, which raises the cellular strain energy to its homeostatic level, and a photoactivation stress $\sigma_{ij,act}(t)$ describing the additional time-dependent stress during and after photoactivation. For the passive properties of the cell layer we choose a Kelvin-Voigt model, i.e., a linear viscoelastic solid, which is defined through the constitutive relation $\sigma_{ij,p} = (1 + \tau_c \partial_t)(\lambda \epsilon_{kk} \delta_{ij} + 2\mu \epsilon_{ij})$ with linear strain tensor $\epsilon_{ij} = (\partial_i u_j + \partial_j u_i)/2$, displacement field u_i , and Lamé parameters λ and μ . Here we use the summation convention for the repeated indices such that $\epsilon_{kk} = \text{tr}(\epsilon)$. In case of strongly spread cells the lateral extent L_c of the cell is usually much larger than its height h_c , such that we make a plane stress assumption, which leads to a two-dimensional model (*i,j* = 1, 2). The Lamé parameters for this case are given by $\lambda = E_c h_c v_c / (1 - v_c^2)$ and $\mu = E_c h_c / (2(1 + v_c))$. E_c and v_c are the three-dimensional Young's modulus and Poisson's ratio of the cell, respectively, and the effective viscosity will be denoted by η_c , leading to the relaxation time constant $\tau_c = \eta_c/E_c$.

The force balance between the thin cell layer and the substrate reads

$$\partial_j \sigma_{ij}(\mathbf{x}, t) = Y(\mathbf{x}) u_i(\mathbf{x}, t), \quad (1)$$

where Y is the local area density of the spring constants representing the stiffness of the foundation. Through its position dependance, $Y(\mathbf{x})$ can also define the adhesive geometry with $Y(\mathbf{x}) \neq 0$ only where the cell is adhered. We here consider two different pattern geometries, the disc pattern (Fig. 1 *a*) where the cell is fully adhered, and the hazard pattern (Fig. 3 *a*) that leads to an organization of the actin cytoskeleton into three domains in a triangular shape. Motivated by the actin images we introduce the polarization of the actin cytoskeleton by making the active motor stress tensor orientation dependent

$$\boldsymbol{\sigma}_m(\varphi) = (\sigma_{bck} + \sigma_{act}(t)) \begin{pmatrix} \cos^2(\varphi) & \frac{1}{2} \sin(2\varphi) \\ \frac{1}{2} \sin(2\varphi) & \sin^2(\varphi) \end{pmatrix}, \quad (2)$$

where φ denotes the orientation of the internal stress fibers with respect to the coordinate system. Furthermore, we assume that both background stress and photoactivation stress pull in the same direction. Since photoactivation only leads to little changes in the cytoskeleton, the direction of pulling is not changed during photoactivation, but its strength is. In the case of cells adhering to the disc pattern we set $\varphi_{DP} = \pi/2$ (Fig. 2 *b*) and in the case for cells plated on the hazard pattern we define three independent (unidirectional) stress regions arranged in a triangular fashion with $\varphi_{1,HP} = -\pi/3$, $\varphi_{2,HP} = \pi/3$, and $\varphi_{3,HP} = 0$ (Fig. 3 *a* and *d*).

For the time course of the photoactivation stress we choose a double sigmoidal profile (Fig. 2 *d*) of the form

$$\sigma_{act}(t) = \frac{\sigma_0}{1 + \exp\left(-\frac{t-t_{act}}{\tau_{act}}\right)} \left(1 - \frac{1}{1 + \exp\left(-\frac{t-t_{rel}}{\tau_{rel}}\right)}\right) \quad (3)$$

with peak activation stress σ_0 , stress activation and relaxation constants τ_{act} and τ_{rel} , respectively, and with the centers of the activation and relaxation sigmoid t_{act} and t_{rel} , respectively. Other activation profiles combined with the KV model and other constitutive laws are discussed in the [supporting material](#) where we also justify our choice of the double sigmoid activation profile.

Numerical implementation

All simulations were carried out using the open-source finite element software FEniCs (52). We solve the weak form of Eq. (1) which reads

$$\int_{\mathcal{Q}} \boldsymbol{\sigma} : \frac{1}{2} (\nabla \mathbf{v} + \nabla \mathbf{v}^T) dx + \int_{\mathcal{Q}} Y \mathbf{u} \cdot \mathbf{v} dx = 0, \quad (4)$$

where \mathcal{Q} denotes the circular cell geometry on which a triangular mesh was generated and \mathbf{v} a vector valued test function. As no stresses are applied at the boundary of the cell, we impose zero stress boundary conditions, $\boldsymbol{\sigma} \cdot \mathbf{N} = 0$ on $\partial \mathcal{Q}$. We further impose the Dirichlet boundary condition $\mathbf{u} = \mathbf{0}$ at the midpoint of the cell.

RESULTS

Larger cells produce more strain energy in response to transient RhoA activation

To investigate how cells react to fast transient activation of the contractile actomyosin system, we coupled time-resolved force imaging with optogenetic stimulations. Our strategy was to trigger the activation of the small GTPase RhoA, the major regulator of cellular contraction (53). We used previously described NIH3T3 cells stably expressing a Cry2-CIBN optogenetic probe to dynamically control the localization of ArhGEF11, an upstream regulator of RhoA, by using blue light (31). To avoid cell shape variability that invariably occurs on homogeneous substrates, we used soft micropatterning to restrict opto-3T3 fibroblasts to disc-shaped fibronectin micropatterns printed on soft (4.47 kPa) polyacrylamide hydrogels of increasing areas (500, 1000, 1500 μm^2) (Fig. 1 *a*). The cells spontaneously polarized on these isotropic patterns, with neighboring stress fibers being approximately parallel. Single focal adhesions grow to larger sizes with increasing cell size, but even on the small islands we always observed a polarized actin cytoskeleton. Using traction force microscopy, we found that the cell forces are localized at the cell periphery, as reported before for well-adhered cells (46,48). Contour plots of the displacement fields clearly demonstrate the dipolar character of single cells, even on the small islands (Fig. 1 *b*) (54). Plots along the indicated lines show that the displacement increases with cell size and decays from the edge inward (Fig. 1 *c*). We define the decay length l_d as the distance on which

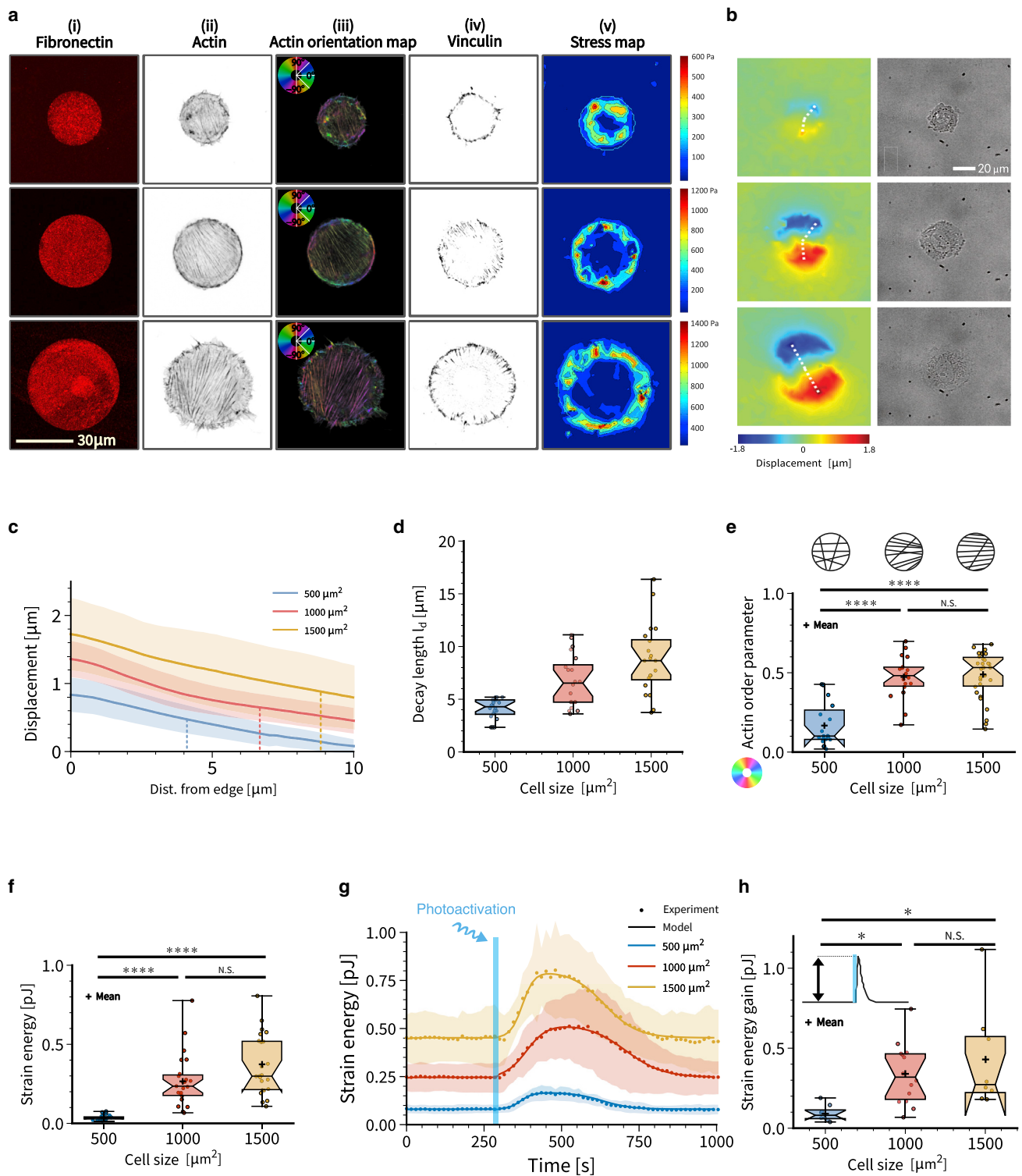


FIGURE 1 Cell size is the major determinant of strain energy and strain energy gain during photoactivation. (a) From left to right: (i) disc-shaped fibronectin micropatterns on polyacrylamide hydrogels with increasing surface area. The patterns cover an area of 500–1000–1500 μm^2 . (ii) Individual actin-labelled cells. (iii) Quantification of the actin orientation by orientation map. The color-coded maps show the angle of oriented features in the image from -90° to 90° (see materials and methods). Larger cells are more polarized. (iv) Adhesion pattern from vinculin staining. The contrast of the vinculin images is enhanced to facilitate visualization of small and thin focal adhesions. (v) Results for traction force microscopy. Traction forces are localized at the cell contour. (b) Exemplary substrate deformation map and bright-field images. Cells show dipolar traction patterns. Substrate deformation is larger for larger cells. (c) Substrate displacement measured with respect to distance from the cell edge along the lines in (b). Vertical lines indicate the mean values of the decay lengths l_d defined by the half-decay of the displacement. (d) Decay length l_d for cells on different pattern sizes. (e) Global cellular actin fiber alignment

(legend continued on next page)

displacement decays to half of its maximal value (vertical lines). This quantity increases with cell size (Fig. 1 *d*), consistent with the observation that the adhesions are larger on the larger islands. Evaluation of the nematic actin order parameter shows that it first increases and then plateaus with cell size (Fig. 1 *e*). This ordering process should also increase the level of force applied to the substrate (55). Indeed we found that, in steady state, cell strain energy increases as a function of cell size (Fig. 1 *f*), as described previously in other studies (48,56–58) and explained theoretically by the increased size of the contact area at constant local contractility (44,46,48,50,51).

We next started to photoactivate the cells. Upon one 100 ms long photo-activation pulse, cell strain energy quickly increased (around 2 min) before slowly relaxing (6–8 min) (Fig. 1 *g*; Videos S1–S3). Very strikingly, cell strain energy recovered its original baseline level with near perfect precision. This suggests that the reaction-diffusion system defined by the membrane-bound part of the Rho system has a well-defined steady state (8,31) and that during optogenetic activation there are no significant changes to the cytoskeleton that modify force generation once this steady state is reached again (Video S4). However, the setpoint of this homeostatic system depends strongly on cell shape. We measured an average strain energy baseline of 0.08, 0.26, and 0.45 pJ on small ($500 \mu\text{m}^2$), medium ($1000 \mu\text{m}^2$), and large ($1500 \mu\text{m}^2$) micropatterns, respectively (Fig. 1 *g*), reflecting the higher pre-stress achieved at higher spread area (Fig. 1 *g*). We then quantified the relative strain energy increase upon photoactivation (RSI, maximum peak value minus baseline strain energy). The RSI upon 100 ms blue light stimulation was only 0.09 pJ for cells spread on small micropatterns, but reached 0.30 and 0.42 pJ on medium and large micropatterns, respectively (Fig. 1 *h*). Thus, optogenetic activation was able to nearly double cell force, and did so in proportion to the cell's level of pre-stress.

A mathematical model can decouple optogenetic activation and force generation

The input-output relation measured experimentally convolutes the optogenetic activation through the Rho system with the force generation by the actomyosin system. To decouple these two processes and to achieve a quantitative description, we developed a mesoscopic mathematical model. In such a mesoscopic model, one avoids unknown microscopic details and focuses on the continuum scale in which subcellular actin assemblies generate stresses in the

kPa range. An established mathematical model of this kind is the continuum mechanics of a thin contractile film with active stresses (44,46,48,50,51). Because here we deal with time-dependent processes, this modeling approach has to be extended now by time-dependent active stresses and viscoelastic material properties. Motivated by the experimental observation that, after optogenetic activation, cells return to their baseline stress (Fig. 1 *g*), we assume that the material law for the cell cannot be purely viscous and must contain a strong elastic element. We therefore model the cell as a thin viscoelastic layer of the Kelvin-Voigt type, which describes a solid in parallel with a viscous element (Fig. 2 *a* and supplement). Optogenetic activation is modeled by an increase of the active tension acting in parallel to the elastic and viscous elements. As alternatives to this material law, we also considered active versions of the Maxwell model, which describes a fluid with an elastic element in series, as well as of purely elastic material (supporting material). Using finite element calculations in the open software package FEniCS, we then implemented these material laws for thin contractile sheets that are attached to an elastic foundation with the geometry of interest and locally have a polarized actin cytoskeleton (supporting material). For the circular discs used in Fig. 1, which show clear polarization for all sizes, we use contraction in one direction (Fig. 2 *b*). Thus, our mesoscopic mechanical model can account for both cell size and actin architecture. Although the simulated traction patterns (Fig. 2 *b*) are sharper than the experimentally measured ones (Fig. 1 *a*), our model reflects very well the dipolar character of the polarized cells on the islands.

To parametrize this model, we make use of the fact that it can be solved analytically for isotropic contraction of a circular disc (44,50,51,59). From this calculation, the force localization length l_p emerges as a central quantity that is defined by the ratio of cell to substrate stiffness (supporting material). This length can be understood as the typical length scale on which the deformation decays that is caused by a localized force, as quantified before in Fig. 1 *d* by the decay length l_d . Using consensus values for the material parameters of cells, the measured substrate strain energy around pJ and the physical dimensions of our patterns, one can parametrize the model almost completely (supporting material). Only background stress σ_{back} and localization length l_p are determined by fitting to the experimentally measured strain energy (model results tabulated in supporting material). We find that simulated substrate displacements u , force localization length l_p , and substrate strain energies E_s show the same increase with cell size as found

for cells spread on each disc size. This is represented by the actin order parameter. (f) Static strain energy for cells spread on the three different disc sizes. Using a one-way ANOVA test, significant difference is found between cells spread on $500 \mu\text{m}^2$ pattern and the other two bigger sizes. (g) Quantification of the mean strain energy over time for cells on the different disc sizes subjected to one light pulse of 100 ms. (h) Strain energy increase for every activated cell on the three different disc sizes. Calculation is made by subtracting the strain energy value before activation to the highest strain energy value obtained after light activation. To see this figure in color, go online.

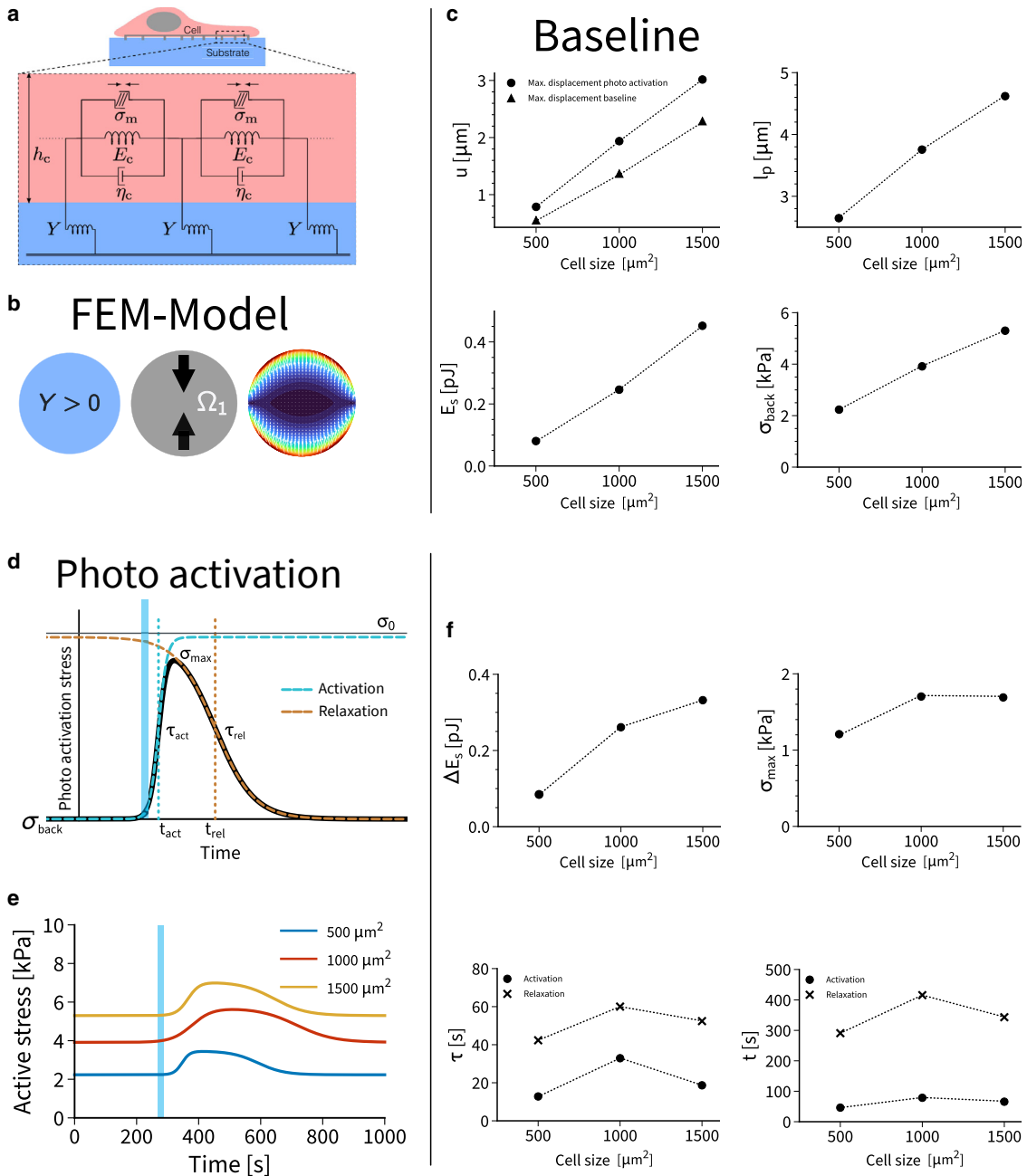


FIGURE 2 A mathematical model decouples activation and force generation. **(a)** The active Kelvin-Voigt model describes a viscoelastic solid with active stresses, which here are controlled by optogenetics. The cell on a soft substrate is modeled as a thin contractile sheet coupled to an elastic foundation. **(b)** Finite element modeling is used to implement the model for anisotropic cell organization like a polarized cell on a disc pattern. The resulting traction patterns resemble the experimentally observed ones. **(c)** The model predicts the variation of displacements, strain energies, localization lengths and background stresses as a function of cell size in very good agreement with experimental observations. **(d)** Photoactivation is modeled by a double sigmoid. **(e)** The model predicts the internal dynamics of the active stresses that cannot be measured directly. **(f)** Predicted values for strain energy gain, gain in active stress, time constants, and sigmoid centers. The model suggests a strong asymmetry between activation (fast) and relaxation (slow). In addition, it reveals peaked values for intermediate cell size. To see this figure in color, go online.

experimentally (Fig. 2 c). The most important result from the model is the background stress σ_{back} , which can only be extracted with the help of the model and has a typical value of 4 kPa (Fig. 2 c). The values for σ_{back} are in good agreement with earlier results from monolayer stress micro-

scopy (60) and tissue stretching experiments (61). In detail, we find $(\sigma_{\text{back}}, l_p) = (2.23 \text{ kPa}, 2.65 \mu\text{m})$, $(\sigma_{\text{back}}, l_p) = (3.91 \text{ kPa}, 3.75 \mu\text{m})$, and $(\sigma_{\text{back}}, l_p) = (5.30 \text{ kPa}, 4.62 \mu\text{m})$, respectively, for the three different disc sizes studied here (Fig. 2 c). Thus, larger systems have larger local

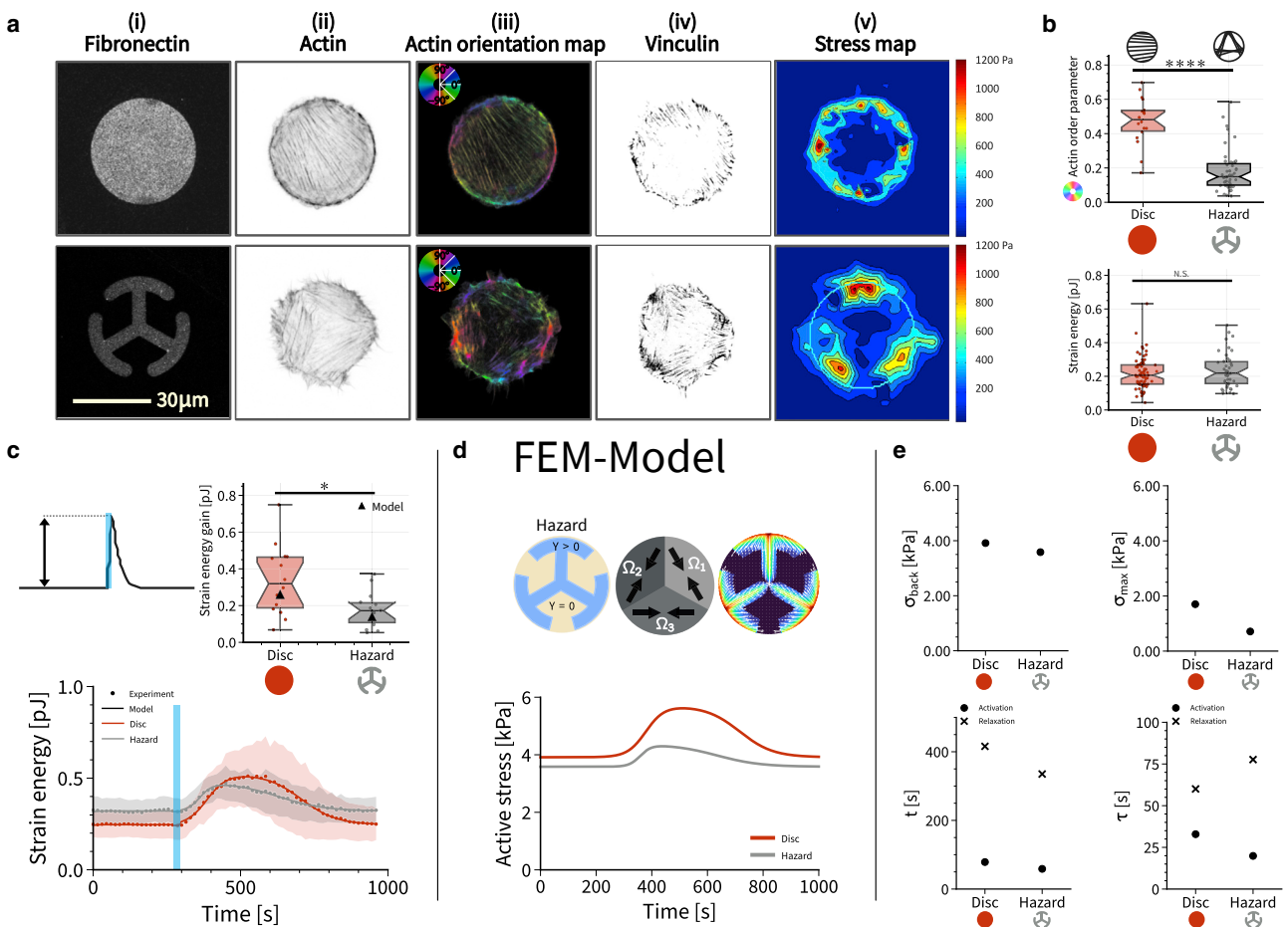


FIGURE 3 Actin architecture modulates magnitude and variability of strain energy gain during activation. (a) From left to right: (i) $1000 \mu\text{m}^2$ disc shaped and hazard shaped fibronectin micropatterns on polyacrylamide hydrogels. (ii) Actin staining. (iii) Actin orientation map. (iv) Adhesion pattern from vinculin staining. The contrast of the vinculin images is enhanced to facilitate visualization of small and thin focal adhesions. (v) Traction stress map. (b) Actin order parameter and strain energy for cells spread on disc or hazard micropatterns. Despite the differences in actin organization, the static strain energy for cells spread on the disc and the hazard shapes is very similar. Using a one-way ANOVA test, significant difference is not found between the two cases. (c) Normalized quantification of the mean strain energy over time for cells on both shapes subjected to one light pulse of 100 ms. (d) The model reveals that internal stresses are very different during activation. (e) Model parameters reveal large differences despite similar strain energies. To see this figure in color, go online.

stresses (larger σ_{back}), possibly because their actin cytoskeleton is better developed, and there is more adhesion (larger l_p), possibly because the FAs are larger, as can be seen in Fig. 1 a. We also note that the orders of magnitude can be predicted from the analytically solvable model for an isotropic contractile disc ([supporting material](#)). Motivated by the theory, we also performed exponentially decaying fits to the experimental data from Fig. 1 c (Fig. S1 a). All three measures for the displacement decay (half-maximum in Fig. 1 c, exponential fit to the same data in Fig. S1 a and model-fit to baseline in Fig. 2 c) show similar values and the same increasing trend with increasing cell size (Fig. S1b).

We next addressed the dynamics of force generation, which is triggered by the optogenetic activation. This process depends on the reaction rates and diffusion constants of the Cry2/CIBIN, Rho, and actomyosin systems and therefore a complete mathematical model is challenging

([31](#)). To arrive at an effective and computationally efficient mathematical description of the time course of the optogenetic activation that gives good fits to the experimental data, we considered different scenarios and found that the best results are obtained by a double-sigmoid profile that is characterized by four timescales: while t_{act} and t_{rel} describe the absolute times after onset of stimulation at which the signal rises and falls, respectively, τ_{act} and τ_{rel} describe the corresponding slopes (Fig. 2 d and [supporting material](#)). In our model, we introduce an internal stress σ_0 that is generated in addition to the background stress σ_{back} after optogenetic activation (uppermost line in Fig. 2 d); however, the physically relevant stress is the maximal value σ_{max} obtained at the peak. By combining the Kelvin-Voigt mechanical model with the double-sigmoid activation curve and fitting for additional stress σ_0 and the four timescales t_{act} , t_{rel} , τ_{act} , and τ_{rel} , we were able to achieve excellent fits to the experimental

data (solid lines in Fig. 1 g). A plot of the active stress in Fig. 2 e shows that the time delay between myosin activation and substrate strain generation is very small, reflecting that the cells are well anchored to the micropatterns and that the elastic part of the cell material dominates over the viscous one. As for the baseline part, fitting the model (Fig. 2 f) gives exactly the experimentally measured values for changes in substrate strain (Fig. 1 h). In addition, we now get predictions for σ_{\max} and the different timescales (Fig. 2 f). Interestingly, the four timescales show peak values for the intermediate cell size of $1000 \mu\text{m}^2$, possibly related to the observation that this value is a typical steady-state spreading area for cells on soft substrates (62). For this optimal pattern size, the cell cannot only achieve a very large peak stress σ_{\max} , it also sustains it for a longer time. Most importantly, we find that τ_{act} (around 20 s) is always much smaller than τ_{rel} (around 50 s), showing that activation is much faster than relaxation, a property that most likely is caused by the reaction-diffusion system of GEF and Rho (31).

Actin architecture determines the efficiency of force production during optogenetic activation

Until now, we have only considered uniformly polarized cells on disc patterns. However, in general, the actin cytoskeleton organizes itself in a complex manner in response to external cues and as a function of spreading history (63). To investigate this relationship between force generation and the organization of the actin cytoskeleton, we next designed a “hazard” micropattern, which has the same convex hull as the disc pattern, but consists of three T-shaped branches emanating from the center (Fig. 3 a). This micropattern induced a very different organization of the actin cytoskeleton, namely three domains of parallel stress fibers rather than one. As a result, the global nematic actin order parameter is now much lower, because different orientations exist in the same cell, making it effectively more isotropic (Fig. 3 b). Surprisingly, however, the strain energies measured by traction force microscopy were rather similar for disc and hazard patterns (Fig. 3 b).

We next measured the dynamic response to blue light stimulation for cells spread on disc versus hazard micropatterns (Fig. 3 c; Videos S5 and S6). The speed of cell contraction was similar on both micropatterns, however, cells on discs, presenting an anisotropic, dipolar actin cytoskeleton, exerted a greater response to photo-activation in terms of force amplitude, with a time to peak of 3.43 ± 0.83 min and an RSI of 0.35 ± 0.05 pJ, and without any change to the cytoskeleton organization during activation (Video S7). Cells on hazard patterns, with a more isotropic, tripolar actin organization, responded with a time to peak of 2.71 ± 1.02 min and an RSI of 0.18 ± 0.02 pJ. The variability of the strain energy gain was higher on the disc than on the

hazard pattern (Fig. 3 c), similar to the results for the background strain energy (Fig. 3 b). To verify that the observed responses in terms of force production were not affected by differences in the fibronectin adhesive area available to the cells, we used a ring-shaped micropattern that has an adhesive area close to the hazard micropattern and measured both the total adhesive area of the cells (quantified via vinculin staining) and the efficiency of force production. We found no significant differences in the total area occupied by focal adhesion on the three different shapes (Fig. S1 c–g). Interestingly the ring-shaped micropattern induced an actin organization close to the one observed on the disc. Together these results demonstrate that the actin architecture is a very important determinant of force generation during optogenetic activation.

We next used the mathematical model to plot active stress for both patterns (Fig. 3 d). In marked contrast to the situation with the baseline stress, we now find that the hazard pattern needs much less additional stress during activation to generate the measured displacements and strain energies. This suggests that the differently organized focal adhesions provide better force transmission from the cell to the substrate; indeed the value for the localization length is smaller for the hazard pattern (supporting material). Fig. 3 e shows the results of the fitting procedure. Both σ_{back} and σ_{\max} are smaller for the hazard pattern, demonstrating that local force generation is weaker if the actin cytoskeleton is less polarized, but that force transmission is increased, because the resulting strain energy is similar. While the centroids t are rather similar for disc and hazard, the local times τ are clearly more distinct, revealing an increased asymmetry between activation and relaxation on the hazard pattern. This suggests that the reaction-diffusion system underlying the Rho response is differently organized in the cells on the hazard pattern, for which both the actin cytoskeleton and the adhesion system are more structured.

Repeated activation reveals saturation of the Rho system

We finally used our mathematical model to test the limits of activation and to study the role of the duration of the activation pulse. We subjected the cells to a series of photoactivation pulses of increasing duration (Fig. 4 a). For each pulse we specify pulse length and injected energy density. Again we observed a well-defined setpoint, as for the single pulse activation from Fig. 1 g. The disc pattern gave larger strain energies, but also had a much larger variability, again as observed above. The stress values extracted with the help of the model (Fig. 4 b) show clear saturation with increased activation times (Fig. 4 c). Surprisingly, the responses for disc and hazard patterns saturated for similar values of the pulse duration (around 25 ms), while the absolute values for the maximal values differ strongly (1.81 kPa for disc and 0.84 kPa for hazard). The higher value for the

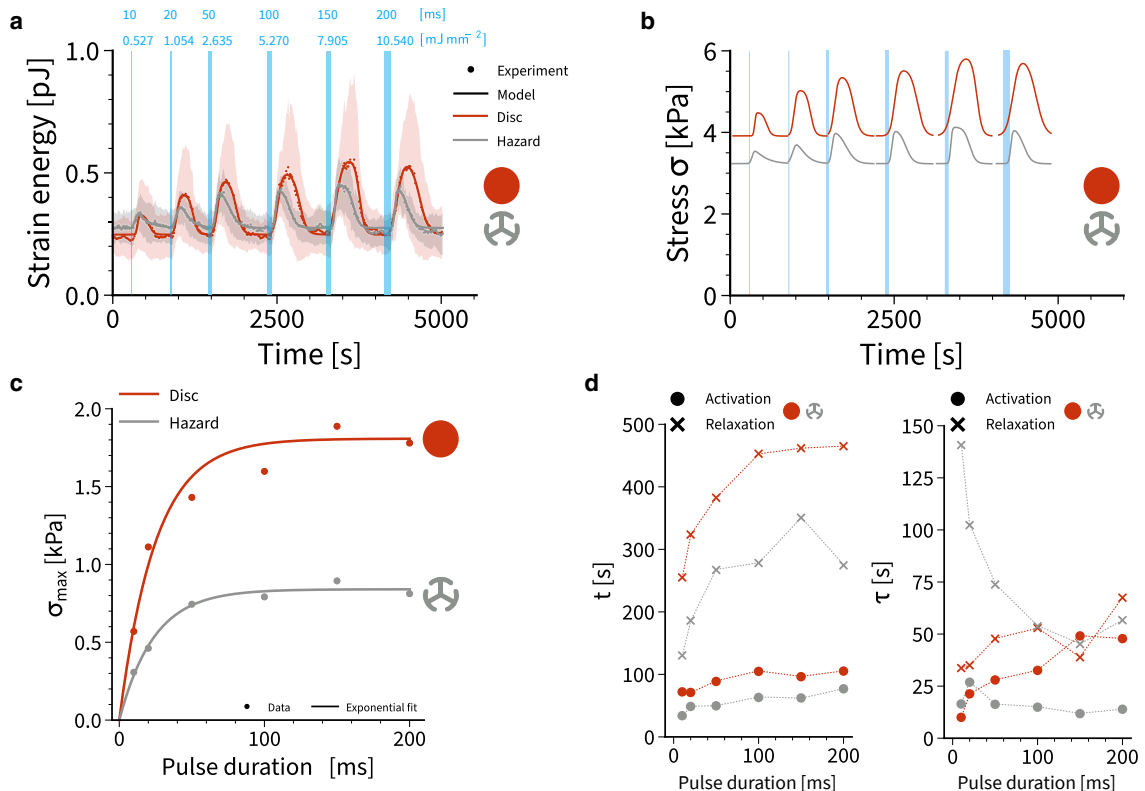


FIGURE 4 The dynamics of photoactivation strongly depend on actin architecture. *(a)* Strain energy during a series of photoactivation pulses of increased duration (represented by stripe width). Dotted lines show mean values, shaded regions correspond to standard deviations and full lines show model fits. The curves represent averages of seven disc and hazard patterns. For each pulse we specify pulse duration and injected energy input. *(b)* Active stresses extracted from the model. *(c)* Maximal active stresses extracted from the model for the two different patterns reveal saturation at 25 ms pulse duration. Solid lines are exponential fits. *(d)* Sigmoid centers t and time constants τ for activation and relaxation for disc and hazard. There is a strong difference between the two actin architectures, reflecting the different internal organization of the cell. To see this figure in color, go online.

disc had to be expected from the more polarized actin organization. The fits of the double-sigmoidal activation profiles revealed very surprising internal dynamics (Fig. 4 *d*). The activation centroids for both patterns are approximately constant around values of 80 s for disc and 50 s for hazard, respectively, and thus independent of PA duration. However, the relaxation centroid location first increases with increasing PA duration and saturates at around 460 s for disc and 270 s for hazard, respectively (disregarding the apparent outlier at 150 ms for the hazard pattern). In contrast, the activation and relaxation timescales for the disc pattern both slightly increase with increasing PA duration and the earlier observed asymmetry between activation and relaxation in the hazard pattern (Fig. 3 *e*) can be observed especially well at smaller PA durations, as the activation time constant for the hazard stays constant at around 15 s while the relaxation time decreases with increasing PA duration. Together these results suggest that the internal actin organization strongly influences the way in which stress decays, despite the fact that it always relaxes to the same tensional setpoint. Given the nontrivial dependence of the relaxation time constant on PA duration and the different relaxation dynamics between cells on hazard and

disc patterns, we conclude that the two patterns must have very different local dynamics of their actomyosin systems.

DISCUSSION

Cells are active adaptive materials whose response to external physical cues has been extensively studied before harnessing advances in micropatterning and biofunctionalization (64). It has been established that cells respond very sensitively to the stiffness, geometry, and topography of their extracellular environment, using cell-matrix adhesions as signaling hubs (65). However, at the same time cell behavior has to be robust in regard to changes in their mechanical environment. A large body of experimental observations suggest that cells do adapt to their mechanical environment mainly by keeping their tension constant (tensional homeostasis) (19). The exact details of this adaptation response might depend on cell type and the exact nature of the environment; for example, it appears that the adaptation response is different if cell-matrix adhesions can rearrange (21) or not (20). Here, we demonstrated by combining micropatterning, elastic substrates, and non-neuronal optogenetics that cell traction forces return to baseline with near-perfect precision after a transient

perturbation in their control structure for force generation, but that the underlying molecular processes strongly depend on the exact organization of the actin cytoskeleton.

Our work builds on recent advances in optogenetics. Most of the current approaches used in the study of single-cell homeostasis can be grouped into two main classes: 1) biological perturbations (e.g., pharmacological inhibition, knockouts, knockdowns, inducible promoters) and 2) physical perturbations (e.g., fluid flow, AFM indentation, geometrical and adhesive constraints, substrate stretch). However, all of these traditional approaches take time to effect cell changes and usually are applied to the cell as a whole. For example, the common myosin II inhibitor blebbistatin can only be applied to the whole cell at once and needs minutes to decrease force levels. To restore the original level, it has to be washed out again. Therefore, traditional approaches are sometimes hard to control and usually are applied to probe more a steady state of the cell rather than a dynamical situation as it occurs e.g., during development, wound healing, or cancer cell migration. Thus, the main limitation of current approaches is their lack of spatial and temporal control. Non-neuronal optogenetics is a very promising new tool that offers exactly this kind of control (26,27). To interrogate tensional homeostasis with this method, here we have combined optogenetic activation of the actomyosin system with traction force microscopy (32,34). By designing different adhesive micropatterns leading to different organization of the actin cytoskeleton, we were able to show that the actin architecture is the main determinant of the cellular response.

Because force generation and its control by the small GTPases from the Rho family are so closely related in cells, it is very difficult to experimentally separate the two processes. To address this challenge, we have therefore developed a mesoscopic mathematical model that allowed us to deconvolute these two essential aspects of the system. Our model is designed in the spirit of active gel theory (66), but uses a viscoelastic model for solids (Kelvin-Voigt model), as a viscoelastic model for fluids (Maxwell model) cannot fit the experimental data. In the future, this modeling approach might be complemented by a more microscopic approach, e.g., using agent-based models for the actomyosin system (67,68). Because it focuses on the geometrical aspects of the system, our mesoscopic model can nicely explain the effect of cell size and actin domain structure on traction forces, and in addition allows us to couple it to different models of optogenetic simulation. We found that only the double-sigmoid model can fit the experimental data well, because it results in the relatively smooth and symmetric profiles observed experimentally. At the same time, however, it allows us to extract time constants and centroids as a function of actin architecture, which reveal some unexpected differences between the two patterns studied here.

While in the hazard pattern with three families of parallel actin bundles the stress buildup starts earlier in contrast to the disc pattern, the disc pattern with one family of parallel actin

bundles remains activated for a longer period of time, because the stress decrease sets in much later than in the hazard pattern. In addition, the hazard pattern is activated on a faster timescale than the disc pattern, but relaxes much slower for short PA perturbations. This observed asymmetry becomes weaker with increasing PA duration. We also found that both patterns saturate at distinct stresses as a function of photoactivation duration, with the disc pattern reaching a stress plateau approximately twice that of the hazard pattern, indicating that a single system of parallel stress fibers has the highest capability of internal force generation. Interestingly, this does not translate directly into much larger strain energy, because at the same time the adhesion system is differently organized (demonstrated by different values for the force localization length l_p). This suggests that reduced force generation in a more disorganized actin cytoskeleton is offset by better coupling to the environment through focal adhesions.

Our experiments only consider cells in mature adhesion, such that actin cytoskeleton and adhesions do not change during photoactivation. We expect that actin architecture will be much more dynamic if optogenetic stimulation is already applied during the spreading processes. In the future, the optogenetic approach employed here might be used to actually control the spreading process by directing the generation of the actin cytoskeleton in the desired direction. To further explore this direction, it then would be appropriate to bring the model closer to the experiments and to transfer the knowledge on the actin orientation directly into the FEM description. A similar strategy has been followed before in model-based TFM, where both stress fiber and focal adhesion data have been converted into a cell-scale model (69). Here, however, we decided to abstract from these subcellular details and to focus on one transparent FEM model for the whole cell.

In summary, our results suggest that actin architecture is the main determinant of force generation in adherent cells and that it strongly shapes the way the different parts of the Rho pathway work together in the cell, including possibly the diffusion of its soluble components such as the Rho-associated kinase. This also suggests that the organization of the actin architecture during spreading pre-conditions the way cells can later perceive their physical environment, thus adding a new dynamic dimension to the way cells sense their microenvironment.

SUPPORTING MATERIAL

Supporting material can be found online at <https://doi.org/10.1016/j.bj.2023.01.011>.

AUTHOR CONTRIBUTIONS

T.A. performed the experiments, performed data analysis, and wrote the first manuscript draft under the supervision of M.B., T.B., and U.S.S. D.W. and D.P. developed the model under the supervision of U.S.S. and

performed data analysis. I.W. developed the TFM algorithm and measured the orientation of the actin network. P.M. designed the photomasks used to make the micropatterns and provided technical assistance and maintenance for the technical facilities. V.F. performed the analysis and quantification of the adhesion structures. All authors contributed with editing the manuscript and providing fruitful discussions and feedback.

ACKNOWLEDGMENTS

M.B. acknowledges financial support from the French Agence Nationale de la Recherche (ANR) for the PlatForMechanics grant ANR-18-CE14-0037-02, the Inter-s-cal grant ANR-21-CE13-0042-02 and the MechanoSwitch grant ANR-17-CE30-0032-01. U.S.S. acknowledges funding through the DFG (Deutsche Forschungsgemeinschaft) grant MechanoSwitch SCHW 834/2-1. T.B. acknowledges funding through CNRS grants (Actions Interdisciplinaires 2017, DEFI Instrumentation aux limites 2017, Tremplin@INP 2021, PEPS CNRS-INNIS 2021, Lumière Visible et Vie 2022) and the Center of Excellence of Multifunctional Architectured Materials "CEMAM" (no. AN-10-LABX-44-01). We would like to thank Laurent Blanchoin, Manuel Thery, Matthieu Coppey, Simon de Beco, Olivier Destaing, and the whole MicroTiss team for useful discussions and feedback.

DECLARATION OF INTERESTS

The authors declare no competing interests.

REFERENCES

- Discher, D. E., L. Smith, ..., S. Safran. 2017. Matrix mechanosensing: from scaling concepts in 'omics data to mechanisms in the nucleus, regeneration, and cancer. *Annu. Rev. Biophys.* 46:295–315.
- Chan, C. J., C. P. Heisenberg, and T. Hiragi. 2017. Coordination of morphogenesis and cell-fate specification in development. *Curr. Biol.* 27:R1024–R1035.
- Blanchoin, L., R. Boujemaa-Paterski, ..., J. Plastino. 2014. Actin dynamics, architecture, and mechanics in cell motility. *Physiol. Rev.* 94:235–263.
- Koenderink, G. H., and E. K. Paluch. 2018. Architecture shapes contractility in actomyosin networks. *Curr. Opin. Cell Biol.* 50:79–85.
- Banerjee, S., M. L. Gardel, and U. S. Schwarz. 2020. The actin cytoskeleton as an active adaptive material. *Annu. Rev. Condens. Matter Phys.* 11:421–439.
- Burridge, K., and K. Wennerberg. 2004. Rho and Rac take center stage. *Cell.* 116:167–179.
- Ridley, A. J. 2011. Life at the leading edge. *Cell.* 145:1012–1022.
- de Beco, S., K. Vaidžiulytė, ..., M. Coppey. 2018. Optogenetic dissection of Rac1 and Cdc42 gradient shaping. *Nat. Commun.* 9:4816.
- Lessey, E. C., C. Guilluy, and K. Burridge. 2012. From mechanical force to RhoA activation. *Biochemistry.* 51:7420–7432.
- Pertz, O., L. Hodgson, ..., K. M. Hahn. 2006. Spatiotemporal dynamics of RhoA activity in migrating cells. *Nature.* 440:1069–1072.
- Burnette, D. T., L. Shao, ..., J. Lippincott-Schwartz. 2014. A contractile and counterbalancing adhesion system controls the 3D shape of crawling cells. *J. Cell Biol.* 205:83–96.
- Dembo, M., and Y. L. Wang. 1999. Stresses at the cell-to-substrate interface during locomotion of fibroblasts. *Biophys. J.* 76:2307–2316.
- Balabán, N. Q., U. S. Schwarz, ..., B. Geiger. 2001. Force and focal adhesion assembly. *Nat. Cell Biol.* 3:466–472.
- Butler, J. P., I. M. Tolić-Nørrelykke, ..., J. J. Fredberg. 2002. Traction fields, moments, and strain energy that cells exert on their surroundings. *Am. J. Physiol. Cell Physiol.* 282:C595–C605.
- Schwarz, U. S., and S. A. Safran. 2013. Physics of adherent cells. *Rev. Mod. Phys.* 85:1327–1381.
- Dufort, C. C., M. J. Paszek, and V. M. Weaver. 2011. Balancing forces: architectural control of mechanotransduction. *Nat. Rev. Mol. Cell Biol.* 12:308–319.
- Humphrey, J. D., E. R. Dufresne, and M. A. Schwartz. 2014. Mechanotransduction and extracellular matrix homeostasis. *Nat. Rev. Mol. Cell Biol.* 15:802–812.
- Brown, R. A., R. Prajapati, ..., M. Eastwood. 1998. Tensional homeostasis in dermal fibroblasts: mechanical responses to mechanical loading in three-dimensional substrates. *J. Cell. Physiol.* 175:323–332.
- Boudou, T., T. Andersen, and M. Balland. 2019. On the spatiotemporal regulation of cell tensional state. *Exp. Cell Res.* 378:113–117.
- Webster, K. D., W. P. Ng, and D. A. Fletcher. 2014. Tensional homeostasis in single fibroblasts. *Biophys. J.* 107:146–155.
- Weng, S., Y. Shao, ..., J. Fu. 2016. Mechanosensitive subcellular rheostasis drives emergent single-cell mechanical homeostasis. *Nat. Mater.* 15:961–967.
- Hippler, M., K. Weißenbruch, ..., M. Bastmeyer. 2020. Mechanical stimulation of single cells by reversible host-guest interactions in 3D microscaffolds. *Sci. Adv.* 6:eabc2648.
- Weißenbruch, K., J. Grewe, ..., M. Bastmeyer. 2021. Distinct roles of nonmuscle myosin II isoforms for establishing tension and elasticity during cell morphodynamics. *Elife.* 10:e71888.
- Paszek, M. J., N. Zahir, ..., V. M. Weaver. 2005. Tensional homeostasis and the malignant phenotype. *Cancer Cell.* 8:241–254.
- Gulhati, P., K. A. Bowen, ..., B. M. Evers. 2011. mTORC1 and mTORC2 regulate EMT, motility, and metastasis of colorectal cancer via RhoA and Rac1 signaling pathways. *Cancer Res.* 71:3246–3256.
- Guglielmi, G., H. J. Falk, and S. De Renzis. 2016. Optogenetic control of protein function: from Intracellular processes to tissue morphogenesis. *Trends Cell Biol.* 26:864–874.
- Wittmann, T., A. Dema, and J. van Haren. 2020. Lights, cytoskeleton, action: optogenetic control of cell dynamics. *Curr. Opin. Cell Biol.* 66:1–10.
- Weitzman, M., and K. M. Hahn. 2014. Optogenetic approaches to cell migration and beyond. *Curr. Opin. Cell Biol.* 30:112–120.
- Tischer, D., and O. D. Weiner. 2014. Illuminating cell signalling with optogenetic tools. *Nat. Rev. Mol. Cell Biol.* 15:551–558.
- Izquierdo, E., T. Quinkler, and S. De Renzis. 2018. Guided morphogenesis through optogenetic activation of Rho signalling during early Drosophila embryogenesis. *Nat. Commun.* 9:2366.
- Valon, L., F. Etoc, ..., M. Coppey. 2015. Predictive spatiotemporal manipulation of signaling perturbations using optogenetics. *Biophys. J.* 109:1785–1797.
- Valon, L., A. Marín-Llauradó, ..., X. Trepat. 2017. Optogenetic control of cellular forces and mechanotransduction. *Nat. Commun.* 8:14396.
- Wagner, E., and M. Glotzer. 2016. Local RhoA activation induces cytokinetic furrows independent of spindle position and cell cycle stage. *J. Cell Biol.* 213:641–649.
- Oakes, P. W., E. Wagner, ..., M. L. Gardel. 2017. Optogenetic control of RhoA reveals zyxin-mediated elasticity of stress fibres. *Nat. Commun.* 8:15817.
- Staddon, M. F., K. E. Cavanaugh, ..., S. Banerjee. 2019. Mechanosensitive junction remodeling promotes robust epithelial morphogenesis. *Biophys. J.* 117:1739–1750.
- Cavanaugh, K. E., M. F. Staddon, ..., M. L. Gardel. 2020. RhoA mediates epithelial cell shape changes via mechanosensitive endocytosis. *Dev. Cell.* 52:152–166.e5.
- Kamps, D., J. Koch, ..., L. Dehmelt. 2020. Optogenetic Tuning reveals Rho amplification-dependent dynamics of a cell contraction signal network. *Cell Rep.* 33:108467.
- Hadjitheodorou, A., G. R. R. Bell, ..., J. A. Theriot. 2021. Directional reorientation of migrating neutrophils is limited by suppression of

- receptor input signaling at the cell rear through myosin II activity. *Nat. Commun.* 12:6619.
39. Vignaud, T., H. Ennomani, and M. Théry. 2014. Chapter 6 - polyacrylamide hydrogel micropatterning. In *Methods in Cell Biology*. M. Piel and M. Théry, eds Academic Press, pp. 93–116.
 40. Püspöki, Z., M. Storath, ..., M. Unser. 2016. Transforms and operators for directional bioimage analysis: a survey. In *Focus on Bio-Image Informatics*. W. H. De Vos, S. M., and J.-P. Timmermans, eds Springer International Publishing, Cham, pp. 69–93.
 41. Sabass, B., M. L. Gardel, ..., U. S. Schwarz. 2008. High resolution traction force microscopy based on experimental and computational advances. *Biophys. J.* 94:207–220.
 42. Butler, J. P., I. M. Tolic-Nørrelykke, ..., J. J. Fredberg. 2002. Traction fields, moments, and strain energy that cells exert on their surroundings. *Am. J. Physiol. Cell Physiol.* 282:C595–C605.
 43. Tse, J. R., and A. J. Engler. 2010. Preparation of hydrogel substrates with tunable mechanical properties. *Curr Protoc Cell Biol.* 47:10–16.
 44. Edwards, C. M., and U. S. Schwarz. 2011. Force localization in contracting cell layers. *Phys. Rev. Lett.* 107:128101.
 45. Banerjee, S., and M. C. Marchetti. 2012. Contractile stresses in cohesive cell layers on finite-thickness substrates. *Phys. Rev. Lett.* 109:108101.
 46. Mertz, A. F., S. Banerjee, ..., E. R. Dufresne. 2012. Scaling of traction forces with the size of cohesive cell colonies. *Phys. Rev. Lett.* 108:198101.
 47. Banerjee, S., and M. Cristina Marchetti. 2013. Controlling cell–matrix traction forces by extracellular geometry. *New J. Phys.* 15:035015.
 48. Oakes, P. W., S. Banerjee, ..., M. L. Gardel. 2014. Geometry regulates traction stresses in adherent cells. *Biophys. J.* 107:825–833.
 49. Vishwakarma, M., J. Di Russo, ..., J. P. Spatz. 2018. Mechanical interactions among followers determine the emergence of leaders in migrating epithelial cell collectives. *Nat. Commun.* 9:3469.
 50. Hanke, J., D. Probst, ..., S. Köster. 2018. Dynamics of force generation by spreading platelets. *Soft Matter*. 14:6571–6581.
 51. Solowiej-Wedderburn, J., and C. M. Dunlop. 2022. Sticking around: cell adhesion patterning for energy minimization and substrate mechanosensing. *Biophys. J.* 121:1777–1786.
 52. Alnæs, M., J. Blechta, ..., G. N. Wells. 2015. The FEniCS Project Version 1.5, 3. Archive of Numerical Software.
 53. Hall, A. 1998. Rho GTPases and the actin cytoskeleton. *Science*. 279:509–514.
 54. Mandal, K., I. Wang, ..., M. Balland. 2014. Cell dipole behaviour revealed by ECM sub-cellular geometry. *Nat. Commun.* 5:5749.
 55. Gupta, M., B. R. Sarangi, ..., B. Ladoux. 2015. Adaptive rheology and ordering of cell cytoskeleton govern matrix rigidity sensing. *Nat. Commun.* 6:7525.
 56. Tan, J. L., J. Tien, ..., C. S. Chen. 2003. Cells lying on a bed of microneedles: an approach to isolate mechanical force. *Proc. Natl. Acad. Sci. USA.* 100:1484–1489.
 57. Reinhart-King, C. A., M. Dembo, and D. A. Hammer. 2005. The dynamics and mechanics of endothelial cell spreading. *Biophys. J.* 89:676–689.
 58. Tseng, Q., I. Wang, ..., M. Balland. 2011. A new micropatterning method of soft substrates reveals that different tumorigenic signals can promote or reduce cell contraction levels. *Lab Chip*. 11:2231–2240.
 59. Chojowski, R., U. S. Schwarz, and F. Ziebert. 2020. Reversible elastic phase field approach and application to cell monolayers. *Eur. Phys. J. E Soft Matter*. 43:63.
 60. Trepat, X., M. R. Wasserman, ..., J. J. Fredberg. 2009. Physical forces during collective cell migration. *Nat. Phys.* 5:426–430.
 61. Wyatt, T. P. J., J. Fouchard, ..., G. T. Charras. 2019. Actomyosin controls planarity and folding of epithelia in response to compression. *Nat. Mater.* 19:109–117.
 62. Nisenholz, N., K. Rajendran, ..., A. Zemel. 2014. Active mechanics and dynamics of cell spreading on elastic substrates. *Soft Matter*. 10:7234–7246.
 63. Kassianidou, E., D. Probst, ..., S. Kumar. 2019. Extracellular matrix geometry and initial adhesive position determine stress fiber network organization during cell spreading. *Cell Rep.* 27:1897–1909.e4.
 64. Matellan, C., and A. E. Del Río Hernández. 2019. Engineering the cellular mechanical microenvironment – from bulk mechanics to the nanoscale. *J. Cell Sci.* 132:jcs229013.
 65. Geiger, B., J. P. Spatz, and A. D. Bershadsky. 2009. Environmental sensing through focal adhesions. *Nat. Rev. Mol. Cell Biol.* 10:21–33.
 66. Prost, J., F. Jülicher, and J.-F. Joanny. 2015. Active gel physics. *Nat. Phys.* 11:111–117.
 67. Stam, S., S. L. Freedman, ..., M. L. Gardel. 2017. Filament rigidity and connectivity tune the deformation modes of active biopolymer networks. *Proc. Natl. Acad. Sci. USA.* 114:E10037–E10045.
 68. Belmonte, J. M., M. Leptin, and F. Nédélec. 2017. A theory that predicts behaviors of disordered cytoskeletal networks. *Mol. Syst. Biol.* 13:941.
 69. Soiné, J. R. D., C. A. Brand, ..., U. S. Schwarz. 2015. Model-based traction force microscopy reveals differential tension in cellular actin bundles. *PLoS Comput. Biol.* 11:e1004076.

Supplemental information

Cell size and actin architecture determine force generation in optogenetically activated cells

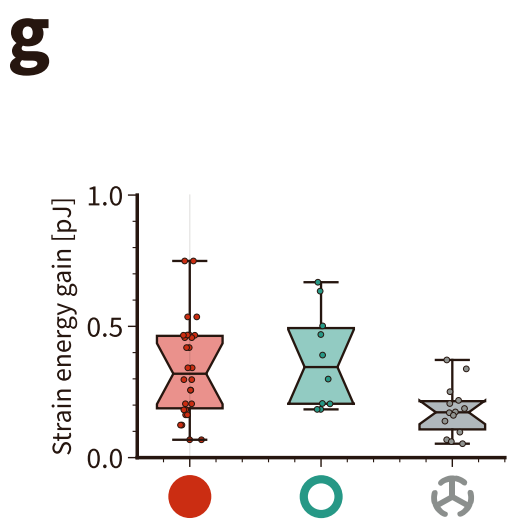
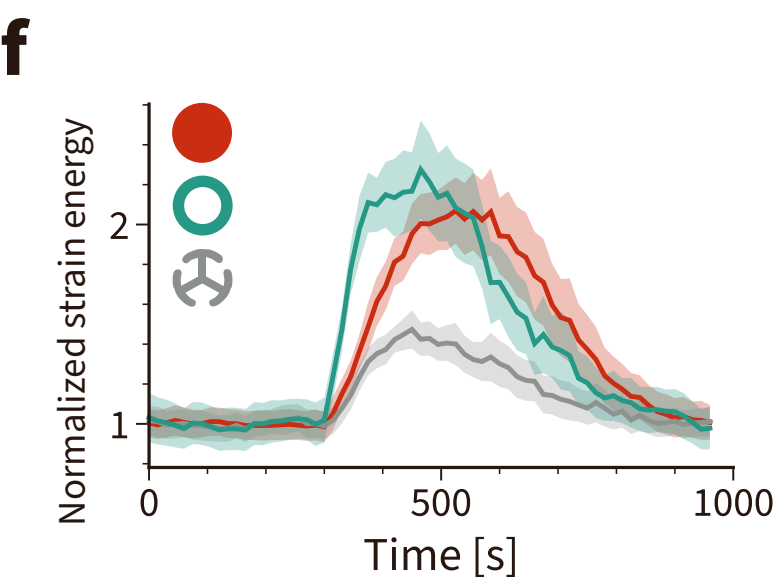
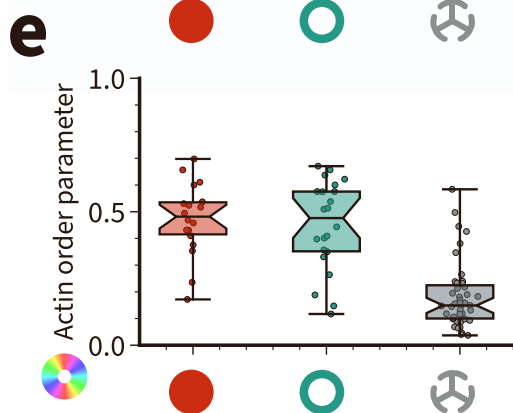
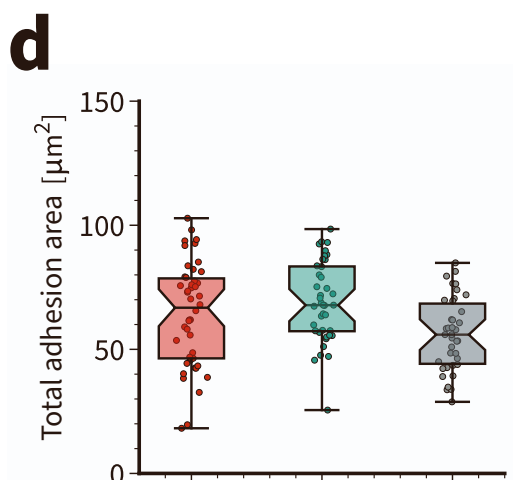
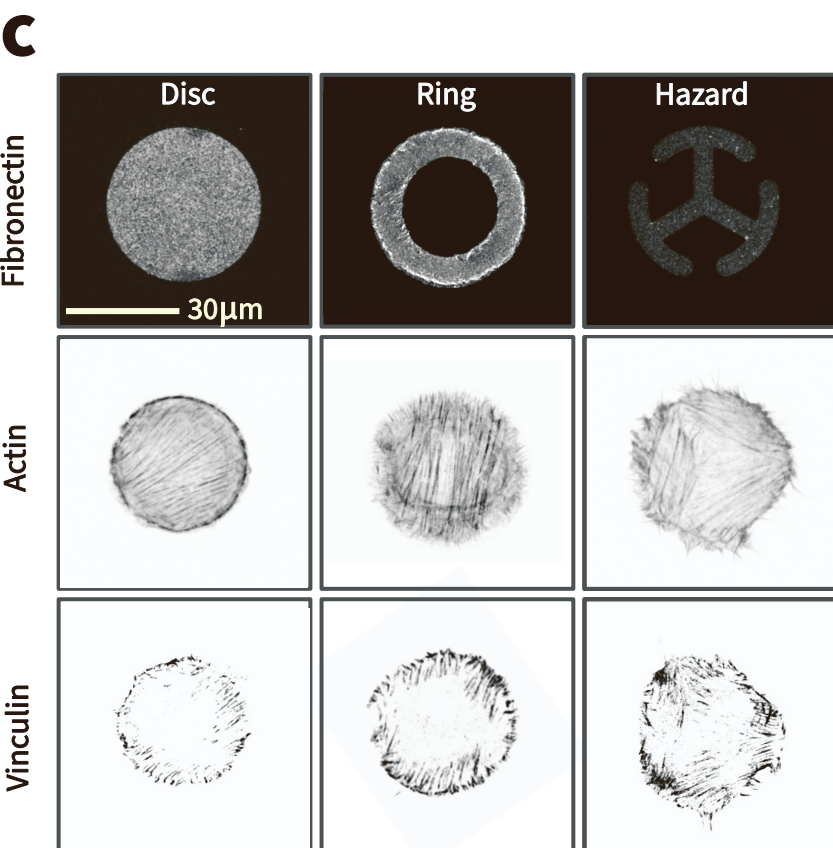
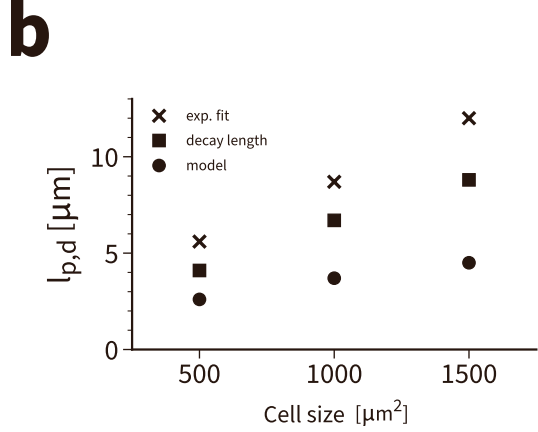
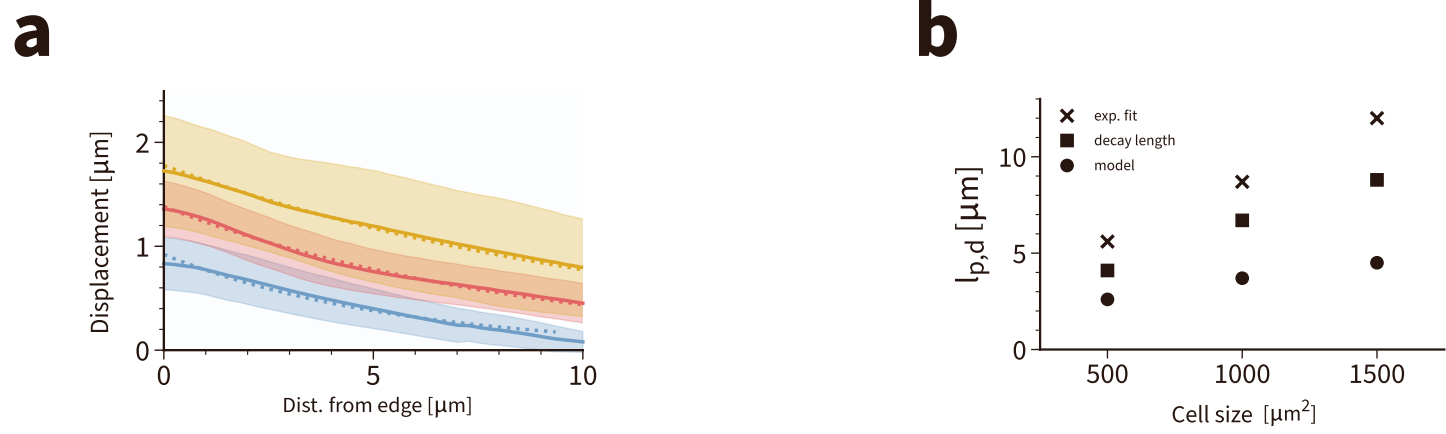
T. Andersen, D. Wörthmüller, D. Probst, I. Wang, P. Moreau, V. Fitzpatrick, T. Boudou, U.S. Schwarz, and M. Balland

Cell size and actin architecture determine force generation in optogenetically activated cells

T. Andersen, D. Wörthmüller, D. Probst, I. Wang, P. Moreau, V. Fitzpatrick, T. Boudou, U.S. Schwarz and M. Balland

Supplemental Figure S1: Cells with similar actin organization display identical force response independently of the pattern adhesive area

(a) Substrate displacement measured with respect to distance from the cell edge along the lines in Fig. 1b. Dotted lines correspond to exponential fits according to the theoretical decay for the displacements. The corresponding values for l_p are 5.6 μm ($500 \mu\text{m}^2$), 8.7 μm ($1000 \mu\text{m}^2$) and 12.0 μm ($1500 \mu\text{m}^2$). (b) Comparison of the three different measures for displacement decay as a function of cell size: half-maximum values from Fig. 1c, exponential fits from Fig. S1a, model-fits to baseline from Fig. 2c. They all show similar values and the same increasing trend with cell size. (c) From left to right: 1000 μm^2 disc, donut and hazard shaped fibronectin micropatterns on polyacrylamide (all patterns cover the same projected area). Individual actin-labelled cells. Individual vinculin staining to reveal focal adhesion localization. The contrast of the vinculin images is enhanced to facilitate visualization of small and thin focal adhesions. (d) Total adhesion area measured as integrated vinculin signal on the 1000 μm^2 disc, donut and hazard shapes. Using a 1-way ANOVA test, significant difference is not found between the three cases. (e) Global cellular actin fibre alignment for cells spread on all fibronectin micropatterns. This is represented by the actin order parameter. Using a 1-way ANOVA test, no significant difference is found between the disc and the donut, however, the hazard pattern displays significant differences with both patterns. (f) Normalized quantification of the mean strain energy over time for cells on all shapes subjected to one light pulse of 100 ms. (g) Strain energy increase for every activated cell on the three different shapes. Calculation is made by subtracting the strain energy value before activation to the highest strain energy value obtained after light activation. Only cells plated on the hazard shaped micropattern displayed lower efficiency in terms of strain energy increase after photoactivation.



Cell size and actin architecture determine force generation in optogenetically activated cells

- Supplemental text -

T. Andersen, D. Wörthmüller, D. Probst, I. Wang, P. Moreau, V. Fitzpatrick,
T. Boudou, U.S. Schwarz and M. Balland

Contents

1 Overview	2
2 Mechanical model	2
3 Substrate strain energy	3
4 Analytical solution for contractile disc	4
5 Numerical implementation	6
6 Adhesive geometry	7
7 Photoactivation	9
8 Parametrization	11
9 Scaling considerations from analytical model	12
10 Effect of actin organization on strain energy level in the model	13
11 Example for python FEM-code for contractile disc	14

1 Overview

Our modelling approach has to combine the following elements: it has to represent the geometry of the adhesive environment of the cell, it has to describe the active mechanical properties of the cell, in particular the effect of photoactivation, and it has to predict the strain energy of the elastic substrate, which shows a characteristic time course after photoactivation. Here we introduce a modelling framework that meets all of these requirements. Our presentation is structured as follows. We first introduce our mechanical model and briefly discuss potential alternatives that we also tested. We then discuss the analytical solutions that are possible for the special assumption of isotropic contractility on a disc pattern. These analytical solution are used to validate our numerical treatment and are helpful to parametrize our model. Next we discuss the numerical implementation of your model, which is needed for the general case of anisotropic contractility. This section also includes a description of how we implement the different adhesive geometries. We then discuss photoactivation, in particular our choice of a double-sigmoid activation curve and potential alternatives. Finally we summarize our parametrization of the model. Here we adopt a mixed strategy. One subset of the parameters is taken from general considerations, and the complementary part is determined by numerical minimizing the loss against experimental data. All parameter values used for the calculations are documented in tables.

2 Mechanical model

We start with the mechanical model. Following earlier work on modelling traction forces as a function of cell geometry [1, 2, 3, 4, 5, 6, 7, 8], we describe the cell as a thin contractile layer that adheres to an elastic foundation (compare Fig. 2a). The force balance between the cell and the substrate reads

$$\partial_j \sigma_{ij}(\mathbf{x}, t) = Y(\mathbf{x}) u_i(\mathbf{x}, t). \quad (1)$$

Here σ_{ij} is the two-dimensional stress in the contractile layer, u_i its displacement field and Y the local area density of the spring constants. Y therefore represents the stiffness of the foundation. Through its position dependance, $Y(\mathbf{x})$ can also represent the adhesive geometry.

For the constitutive law of the contractile layer we choose an active Kelvin-Voigt model:

$$\sigma_{ij} - \sigma_{ij,m} = (1 + \tau_c \partial_t) (\lambda \epsilon_{kk} \delta_{ij} + 2\mu \epsilon_{ij}) \quad (2)$$

with linear strain tensor $\epsilon_{ij} = (\partial_i u_j + \partial_j u_i) / 2$. σ_m denotes the active motor stress, which consists of two contributions: a constant background stress σ_{bck} , which raises the cellular strain energy to its homeostatic level, and a photoactivation (PA) stress tensor $\sigma_{act}(t)$, describing the additional time-dependent stress during PA. λ and μ denote the two-dimensional Lamé coefficients defined by

$$\lambda = \frac{E_c h_c \nu_c}{1 - \nu_c^2}, \quad \mu = \frac{E_c h_c}{2(1 + \nu_c)}. \quad (3)$$

Here E_c and ν_c are the three-dimensional Young's modulus and Poisson's ratio of the cells, respectively, and h_c is the effective thickness of the contractile layer, which is similar to but smaller than cell

thickness. The effective viscosity of the cell will be denoted by η_c and the resulting relaxation time is $\tau_c = \eta_c/E_c$. The limit $\tau_c = 0$ corresponds to the purely elastic case. Because elastic and viscous elements are arranged in parallel in the Kelvin-Voigt model, the corresponding forces simply add up in this equation.

An alternative to the active viscoelastic solid is the active viscoelastic fluid, that is an active Maxwell model, for which we have

$$\frac{\sigma_{ij} - \sigma_{ij,m}}{\tau_c} + (\dot{\sigma}_{ij} - \dot{\sigma}_{ij,m}) = \partial_t (\lambda \epsilon_{kk} \delta_{ij} + 2\mu \epsilon_{ij}) . \quad (4)$$

$\tau_c = 0$ corresponds to the purely viscous case, for which the stress derivative would vanish. Because now elastic and viscous elements for the viscoelastic fluid are arranged in series, they appear here in a different combination than for the viscoelastic solid from Eq. [2]. For this study, we considered all four possible linear models (viscoelastic solid, elastic solid, viscoelastic fluid, viscous fluid), but only the viscoelastic solid was able to describe our experimental data (see below).

In order to solve our model, we have to combine the force balance from Eq. [1] with the constitutive law from Eq. [2]. In general, the resulting equation can only be solved numerically. If one considers the special case of a one-dimensional and purely elastic system ($\tau_c = 0$) with constant stiffness Y and constant active stress σ^m , the resulting equation for the displacement field u is simply

$$\partial_x^2 u - \frac{1}{l_p^2} u = 0 \quad (5)$$

with the newly defined force penetration length l_p and the stiffness Y related by

$$l_p = \left(\frac{E_c h_c}{Y (1 - \nu_c^2)} \right)^{1/2}, \quad Y = \frac{E_c h_c}{l_p^2 (1 - \nu_c^2)} . \quad (6)$$

The force penetration length can be understood as the typical length scale on which a mechanical perturbation decays [1]. In principle this allows us to estimate Y by experimentally measuring l_p .

3 Substrate strain energy

In order to predict the substrate strain energy in our model, we take into account that both the elastic gel and the layer of adhesion molecules connecting it to the cell contribute to the foundation stiffness Y perceived by the cell. Because the stiffnesses of the substrate and of the adhesion layer act in series, we write $1/Y = 1/Y_s + 1/Y_a$. The spring constant density of the substrate is related to its Young's modulus E_s by [2]

$$Y_s = \frac{\pi E_s}{h_{\text{eff}}} \quad (7)$$

where h_{eff} can be estimated as

$$h_{\text{eff}}^{-1} = \frac{1}{h_s 2\pi (1 + \nu_s)} + \frac{1}{L_c} \quad (8)$$

where h_s and ν_s are thickness and Poisson ratio of the substrate, respectively, and L_c is the lateral size of the cell. The stiffness of the adhesion layer can be estimated as $Y_a = k_a/d^2$, where k_a is the molecular stiffness of the adhesion bonds and d the distance between them.

With substrate displacement \mathbf{u}_s , substrate rigidity Y_s and force balance $\mathbf{T} = Y\mathbf{u} = Y_s\mathbf{u}_s$, we now can write for the substrate strain energy:

$$U_s = \frac{1}{2} \int_A \mathbf{T}\mathbf{u}_s dA = \frac{1}{2} \int_A \frac{Y^2}{Y_s} \mathbf{u}^2 dA . \quad (9)$$

This is the central quantity of interest because it is directly measured in the experiments. If the adhesion layer is much stiffer than the elastic substrate, we have $Y = Y_s$ and the energy density is simply $Y_s\mathbf{u}^2/2$.

4 Analytical solution for contractile disc

To estimate the expected values for the strain energy U_s described by Eq. 9 as well as the contractile background stress of the cell, we now turn to an analytical solution of our model that has been derived before for the case of an isotropic contractile disc of radius r_0 [1, 4]. Here we restrict ourselves completely to mechanical equilibrium and neglect viscoelastic effects or non-homogeneous adhesion. The radial displacement u_r for this special case yields [1]

$$u_r(r) = -l_p \frac{\sigma_0 h_c}{\lambda + 2\mu} \cdot \frac{I_1\left(\frac{r}{l_p}\right)}{I_0\left(\frac{r_0}{l_p}\right) - \frac{2\mu}{\lambda+2\mu} \frac{l_p}{r_0} I_1\left(\frac{r_0}{l_p}\right)}, \quad (10)$$

with contractile stress σ_0 , disc height h_c and modified Bessel functions of first kind I_0 and I_1 . The strain energy then reduces to the integral

$$\begin{aligned} U_s &= \frac{Y^2}{2Y_s} \int_0^{2\pi} d\phi \int_0^{r_0} dr r u_r^2 \\ &= \frac{\pi}{Y_s} \cdot \left(\frac{Y l_p \sigma_0 h_c (1 - \nu_c^2)}{E_c h_c} \right)^2 \cdot \frac{\int_0^{r_0} dr r I_1\left(\frac{r}{l_p}\right)^2}{\left(I_0\left(\frac{r_0}{l_p}\right) - (1 - \nu_c) \frac{l_p}{r_0} I_1\left(\frac{r_0}{l_p}\right) \right)^2} = \frac{\pi (\sigma_0 h_c)^2}{2Y_s} \zeta\left(\frac{r_0}{l_p}\right), \end{aligned} \quad (11)$$

using the definition of Y in Eq. 6 and

$$\zeta(x) = x^2 \cdot \frac{I_1(x)^2 + \frac{2}{x} I_0(x) I_1(x) - I_0(x)^2}{\left(I_0(x) - (1 - \nu_c) \frac{1}{x} I_1(x) \right)^2}. \quad (12)$$

The total traction force exerted onto the substrate is given by

$$\begin{aligned} F_{\text{tot}} &= Y \int_0^{2\pi} d\phi \int_0^{r_0} dr r |u_r| \\ &= \frac{2\pi Y l_p \sigma_0 h_c}{\lambda + 2\mu} \frac{\int_0^{r_0} dr r I_1\left(\frac{r}{l_p}\right)}{I_0\left(\frac{r_0}{l_p}\right) - (1 - \nu_c) \frac{l_p}{r_0} I_1\left(\frac{r_0}{l_p}\right)} = \frac{2\pi \sigma_0 h_c}{l_p} \beta\left(\frac{r_0}{l_p}\right), \end{aligned} \quad (13)$$

with

$$\beta(x) = \frac{\pi}{2}x \frac{(L_0(x)I_1(x) - L_1(x)I_0(x))}{I_0(x) - (1 - \nu_c)\frac{1}{x}I_1(x)}, \quad (14)$$

in which L_0 and L_1 denote modified Struve functions.

We can find the two asymptotic limits of the strain energy and the total traction force by investigating ζ and β for the two limits $x \ll 1$ and $x \gg 1$. For $x \ll 1$, the modified Bessel functions can be approximated as

$$I_n(x) \xrightarrow{x \ll 1} \frac{1}{n!} \left(\frac{x}{2}\right)^n, \quad (15)$$

such that

$$\zeta(x) \xrightarrow{x \ll 1} \frac{x^4}{2(1 + \nu_c)^2} + \mathcal{O}(x^5), \quad (16)$$

$$\beta(x) \xrightarrow{x \ll 1} \frac{x^3}{3(1 + \nu_c)} + \mathcal{O}(x^4), \quad (17)$$

and hence

$$U_s \xrightarrow{r_0 \ll l_p} \frac{\pi (\sigma_0 h_c)^2}{4Y_s (1 + \nu_c)^2} \left(\frac{r_0}{l_p}\right)^4, \quad (18)$$

$$F_{\text{tot}} \xrightarrow{r_0 \ll l_p} \frac{2\pi l_p \sigma_0 h_c}{3(1 + \nu_c)} \left(\frac{r_0}{l_p}\right)^3. \quad (19)$$

For $x \gg 1$, any modified Bessel function of the first kind can be approximated as

$$I_n \approx \frac{\exp x}{\sqrt{2\pi x}} \left[1 - \frac{4n^2 - 1^2}{1(8x)} \left(1 - \frac{4n^2 - 3^2}{2(8x)} \left(1 - \frac{4n^2 - 5^2}{3(8x)} (1 - \dots) \right) \right) \right], \quad (20)$$

i.e.

$$I_0 \approx \frac{\exp x}{\sqrt{2\pi x}} \left[1 + \frac{1}{8x} \right] \quad (21)$$

$$I_1 \approx \frac{\exp x}{\sqrt{2\pi x}} \left[1 - \frac{3}{8x} \right] \quad (22)$$

such that

$$\zeta(x) \approx x \frac{64 - \frac{24}{x} - \frac{6}{x^2}}{64 - \frac{48}{x} + \frac{3}{x^2} - \frac{9}{x^3} + \frac{9}{4x^4}} \xrightarrow{x \gg 1} x + \mathcal{O}(x^2), \quad (23)$$

$$\beta(x) \approx x \frac{1 - \frac{7}{8x}}{1 + \frac{1}{8x} - (1 - \nu_c)\frac{1}{x} - \frac{3}{8x^2}} \xrightarrow{x \gg 1} x + \mathcal{O}(x^2), \quad (24)$$

and hence

$$U_s \xrightarrow{r_0 \gg l_p} \frac{\pi (\sigma_0 h_c)^2}{2Y_s} \cdot \frac{r_0}{l_p}, \quad (25)$$

$$F_{\text{tot}} \xrightarrow{r_0 \gg l_p} 2\pi \sigma_0 h_c r_0. \quad (26)$$

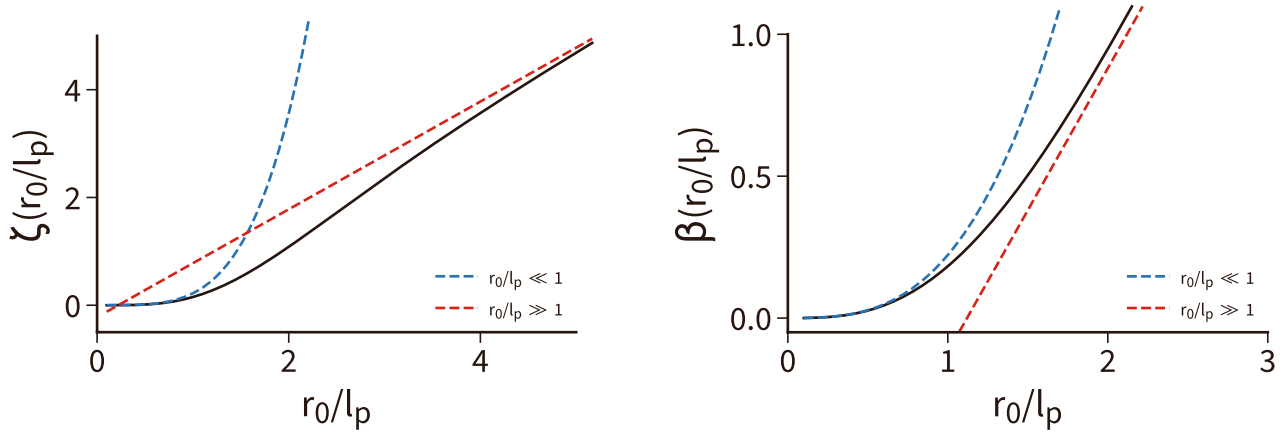


Figure 1: Analytical solution for the substrate strain energy U_s and the total traction force F_{tot} of a uniformly contractile disc as a function of dimensionless disc radius r_0/l_p . Also shown are the two asymptotic limits for small (blue) and large (red) disc radii. For radii r_0 larger than l_p , a linear approximation becomes valid in both cases.

Thus, the asymptotic behavior of the strain energy for $r_0 \gg l_p$ has the same scaling with r_0 as the total force, corresponding to a tension-dominated regime. However, for $r_0 \ll l_p$, the asymptotic behavior of the strain energy and the total force have a different scaling with r_0 , corresponding to an elasticity-dominated regime. As we will see below, in our experiments we always will deal with the tension-dominated regime.

In Fig. 1 we plot the substrate strain energy U_s from Eq. 11 and total traction force F_{tot} from Eq. 13 of the isotropically contracting disc as a function of dimensionless disc radius r_0/l_p (black solid line). We also plot the asymptotic limits for small radius (blue dashed line, Eq. 18) and large radius (red dashed line, Eq. 25). Because in experiments system size will be typically much larger than l_p , we conclude that the linear scaling from the large radius limit best captures the relevant form of the substrate strain energy and total traction force.

5 Numerical implementation

In the general case, no analytical solution is available and our mechanical model has to be solved by means of a finite element (FE) calculation. The weak formulation of Eq. 1 is

$$\int_{\Omega} \boldsymbol{\sigma} : \frac{1}{2} (\nabla \mathbf{v} + \nabla \mathbf{v}^T) \, d\mathbf{x} + \int_{\Omega} Y \mathbf{u} \cdot \mathbf{v} \, d\mathbf{x} = 0, \quad (27)$$

with Ω denoting the meshed cell area (e.g. a disc) and \mathbf{v} a test function. We use the FE-solver FEniCS to calculate the displacements [9]. For symmetry reasons, the Dirichlet boundary condition $\mathbf{u} = (0, 0)$ applies at the midpoint $\mathbf{x} = (0, 0)$.

As a validation of our numerical procedures, we first simulated the contractile disc. Fig. 2 shows that the analytical solution from Eq. 10 and the numerical solution agree very well.

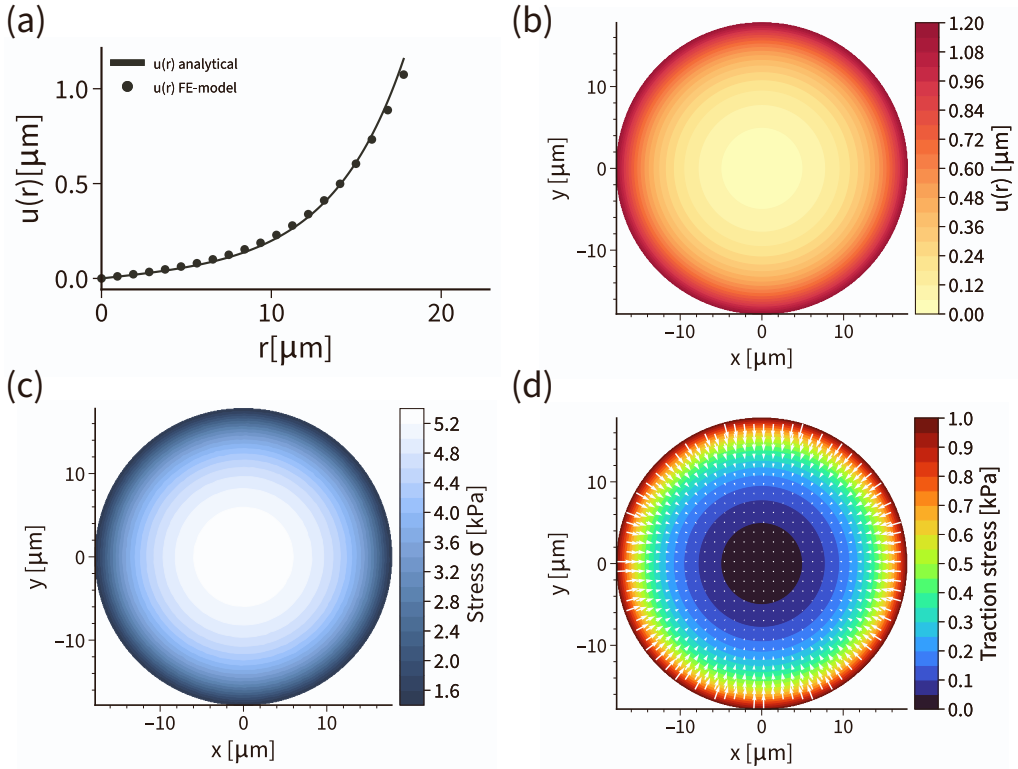


Figure 2: Finite Element Simulation of the isotropic contractile disc. Panel (a) demonstrates the excellent agreement of the numerical FE-implementation with the analytical solution for $u(r)$. Panel (b),(c) and (d) show the displacement field u , total stress σ and the traction stress as obtained by FEM, respectively.

6 Adhesive geometry

An essential element of our treatment is the representation of the adhesive geometry. This can be done by making stiffness Y space-dependent. For example, it has been shown recently that the arrangement of focal adhesions, and thus adhesion geometry, affects the effective substrate stiffness perceived by the cell [8]. For the case of the disc pattern, we represent the effect of the elastic substrate as well as the elastic contribution of the FAs via springs of constant spring stiffness density Y throughout the entire disc. For the hazard pattern, we only introduce springs of stiffness density Y at those positions of the disc at which the cell can form connections to the substrate via its FAs, which is exactly the FN coated area (illustrated in Fig. 3). To simulate this fact, we determine the positions $(x, y)_{Y \neq 0}$, at

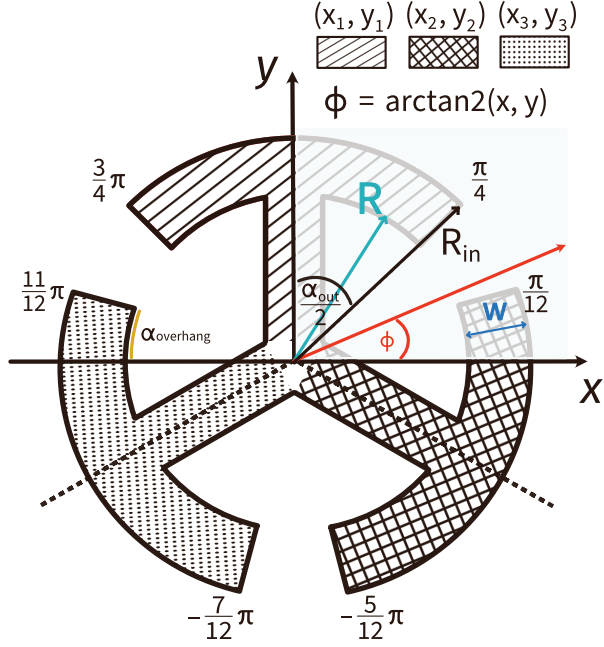


Figure 3: Illustration of the hazard pattern geometry. The relevant angles are described in the main text and implemented in the FEM-simulations.

which the stiffness density Y is non-zero, via:

$$(x, y)_{Y \neq 0} = \left\{ x, y \mid \begin{aligned} & \left[R_{\text{in}} \leq \sqrt{x^2 + y^2} \leq R \wedge \left(\frac{\pi}{2} - \frac{\alpha_{\text{out}}}{2} \leq \arctan2(x, y) \leq \frac{\pi}{2} + \frac{\alpha_{\text{out}}}{2} \right. \right. \\ & \quad \vee -\frac{\pi}{6} - \frac{\alpha_{\text{out}}}{2} \leq \arctan2(x, y) \leq -\frac{\pi}{6} + \frac{\alpha_{\text{out}}}{2} \\ & \quad \vee -\frac{5\pi}{6} - \frac{\alpha_{\text{out}}}{2} \leq \arctan2(x, y) \leq -\frac{5\pi}{6} + \frac{\alpha_{\text{out}}}{2} \\ & \quad \left. \left. \vee \pi - \alpha_{\text{overhang}} \leq \arctan2(x, y) \leq \pi \right) \right] \vee \\ & \left[\sqrt{x^2 + y^2} \leq R_{\text{in}} \wedge \left(\left(-\frac{w}{2} \leq x_1 \leq \frac{w}{2} \wedge y_1 \geq 0 \right) \right. \right. \\ & \quad \vee \left(-\frac{w}{2} \leq x_2 \leq \frac{w}{2} \wedge y_2 \geq 0 \right) \\ & \quad \left. \left. \vee \left(-\frac{w}{2} \leq x_3 \leq \frac{w}{2} \wedge y_3 \geq 0 \right) \right) \right] \}, \end{aligned} \right.$$

with arm width $w = 5 \mu\text{m}$, inner radius $R_{\text{in}} = R - w$ and $\alpha_{\text{out}} = \pi/2$. The remaining parameters are

$$(x_1, y_1) = (x, y)$$

$$(x_2, y_2) = \left(x \cdot \cos\left(\frac{2\pi}{3}\right) - y \cdot \sin\left(\frac{2\pi}{3}\right), x \cdot \sin\left(\frac{2\pi}{3}\right) + y \cdot \cos\left(\frac{2\pi}{3}\right) \right)$$

$$(x_3, y_3) = \left(x \cdot \cos\left(\frac{2\pi}{3}\right) + y \cdot \sin\left(\frac{2\pi}{3}\right), -x \cdot \sin\left(\frac{2\pi}{3}\right) + y \cdot \cos\left(\frac{2\pi}{3}\right) \right),$$

and

$$\alpha_{\text{overhang}} = \frac{5\pi}{6} + \frac{\alpha_{\text{out}}}{2} - \pi \text{ if } \frac{5\pi}{6} + \frac{\alpha_{\text{out}}}{2} > \pi, \text{ otherwise } 0. \quad (28)$$

Eq. 28 accounts for the unsteady jump of the arctan2-function at the function values $-\pi$ and π .

7 Photoactivation

As explained above, the active stress has two components, $\sigma_m = \sigma_{\text{bck}} + \sigma_{\text{act}}(t)$, namely a background stress before PA, and the active stress after PA. We assume that they both pull in the same direction because PA leads to little changes in the cytoskeleton, so the direction of pulling is not changed, but its strength is. We can calculate the anisotropic motor stress tensor σ_m directed along an arbitrary angle ϕ with respect to the x-axis via rotation of a stress tensor with its only non-zero component being $\sigma_{xx} = \sigma_{\text{bck}} + \sigma_{\text{act}}(t)$. Here, σ_{bck} is the background stress and σ_{act} is the time-dependent PA stress. One has

$$\begin{aligned} \sigma_m(\phi) &= \begin{pmatrix} \cos \phi & -\sin \phi \\ \sin \phi & \cos \phi \end{pmatrix} \begin{pmatrix} \sigma_{\text{bck}} + \sigma_{\text{act}} & 0 \\ 0 & 0 \end{pmatrix} \begin{pmatrix} \cos \phi & \sin \phi \\ -\sin \phi & \cos \phi \end{pmatrix} \\ &= (\sigma_{\text{bck}} + \sigma_{\text{act}}) \cdot \begin{pmatrix} \cos^2 \phi & \frac{1}{2} \sin(2\phi) \\ \frac{1}{2} \sin(2\phi) & \sin^2 \phi \end{pmatrix}, \end{aligned} \quad (29)$$

Comparison with the orientation of SFs in cells plated on the two patterns lets us assume a motor stress tensor

$$\sigma_m^{\text{DP}} = \begin{pmatrix} 0 & 0 \\ 0 & \sigma_{\text{bck}} + \sigma_{\text{act}} \end{pmatrix} \quad (30)$$

in the case of the disc pattern (DP) and

$$\begin{aligned} \sigma_{m,\Omega_1}^{\text{HP}} &= (\sigma_{\text{bck}} + \sigma_{\text{act}}) \cdot \begin{pmatrix} 1 & 0 \\ 0 & 0 \end{pmatrix}, \\ \sigma_{m,\Omega_2}^{\text{HP}} &= (\sigma_{\text{bck}} + \sigma_{\text{act}}) \cdot \begin{pmatrix} \cos^2\left(\frac{\pi}{3}\right) & \frac{1}{2} \sin\left(\frac{2\pi}{3}\right) \\ \frac{1}{2} \sin\left(\frac{2\pi}{3}\right) & \sin^2\left(\frac{\pi}{3}\right) \end{pmatrix}, \\ \sigma_{m,\Omega_3}^{\text{HP}} &= (\sigma_{\text{bck}} + \sigma_{\text{act}}) \cdot \begin{pmatrix} \cos^2\left(\frac{\pi}{3}\right) & -\frac{1}{2} \sin\left(\frac{2\pi}{3}\right) \\ -\frac{1}{2} \sin\left(\frac{2\pi}{3}\right) & \sin^2\left(\frac{\pi}{3}\right) \end{pmatrix}, \end{aligned} \quad (31)$$

for the respective regions Ω_1 , Ω_2 and Ω_3 in the case of the hazard pattern (HP).

We consider three possible models for the time course of the PA stress component σ_{act} . The simplest case is the rectangular profile

$$\sigma_{\text{act}}^{\text{rec}}(t) = \begin{cases} \sigma_0 & \text{for } t_0 \leq t \leq t_{\text{act}} \\ 0 & \text{else} \end{cases}, \quad (32)$$

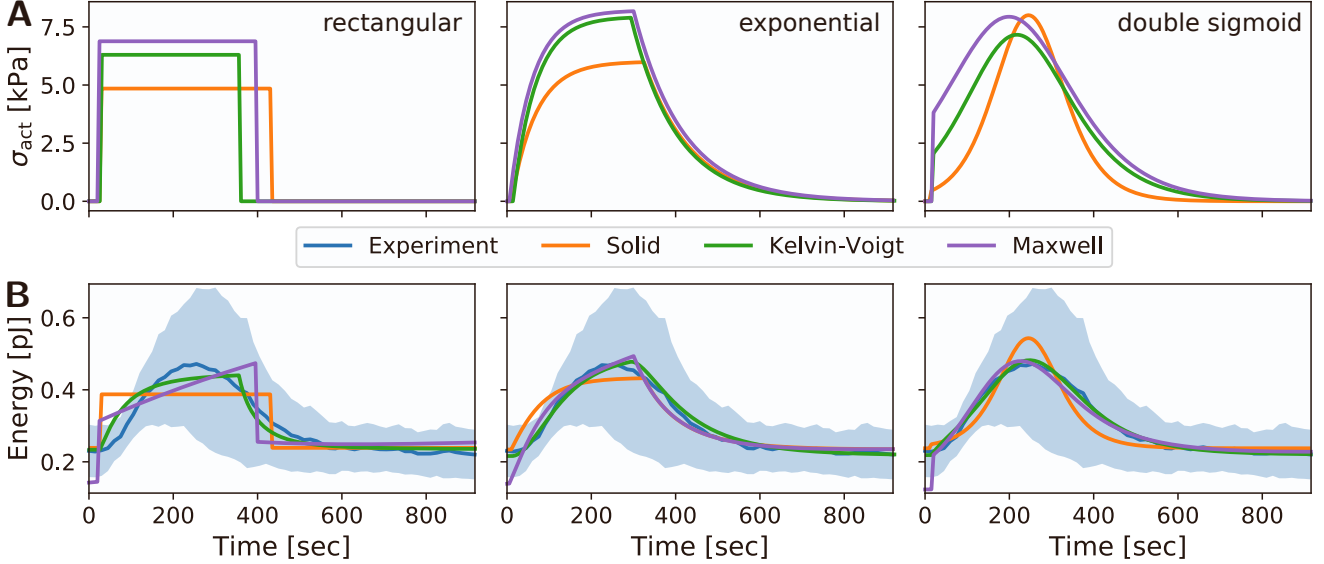


Figure 4: Photoactivation stress profile σ_{act} and the corresponding energy response for the case of a solid, Kelvin-Voigt and Maxwell model. (A) Photoactivation stress profiles σ_{act} used to reproduce the experimentally acquired cellular energy response: rectangular, exponential and double sigmoid profile from left to right. Different curves illustrate the optimized stress profiles for the three models. (B) Corresponding energy responses for the three different stress profiles and continuum models, illustrated on top of the experimental average. *Shaded regions* denote the standard deviation. A Kelvin-Voigt model with a double sigmoid stress profile fits best to the experimental curve.

with peak activation stress σ_0 , PA time point t_0 and duration t_{act} . To account for a delayed response of the activation stress, we introduce the exponential profile

$$\sigma_{act}^{\text{exp}}(t) = \begin{cases} \sigma_0 \left(1 - \exp\left(-\frac{t-t_0}{\tau_{act}}\right)\right) & \text{for } t_0 \leq t \leq t_{act} \\ \sigma_0 \left(1 - \exp\left(-\frac{t_{act}-t_0}{\tau_{act}}\right)\right) \exp\left(-\frac{t-(t_0+t_{act})}{\tau_{rel}}\right) & \text{else} \end{cases}, \quad (33)$$

with stress activation and relaxation times τ_{act} and τ_{rel} . The third stress profile is a double sigmoid function [10]

$$\sigma_{act}^{\text{sig}}(t) = \frac{\sigma_0}{1 + \exp\left(-\frac{t-t_{act}}{\tau_{act}}\right)} \cdot \left(1 - \frac{1}{1 + \exp\left(-\frac{t-t_{rel}}{\tau_{rel}}\right)}\right), \quad (34)$$

with the centers of the activating and relaxing sigmoid t_{act} and t_{rel} . Here, the two time constants and the two time centroids allow us to combine a discontinuous jump at the ascending edge of the PA stress function and a flat stress plateau, as with the rectangular stress profile, with a damped activation and relaxation, as with the exponential stress profile. Thus the sigmoid activation can be considered to be the most general form of an activation profile.

These three different PA-stresses now can be combined with each of the four mechanical models introduced above to select the best model for further analysis. A purely viscous model can be excluded right from the beginning as it would not allow to keep a steady energy state, even in the absence of a PA-signal. In Fig. 4, we show the responses of the three other potential models, each time combined

Fixed parameter	Value
Young's modulus of the substrate E_s	4.47 kPa
Poisson's ratio of the substrate ν_s	0.5
Substrate thickness h_s	50 μm
Lateral cell size L_c	50 μm
Young's modulus of the cell E_c	10 kPa
Viscosity of the cell η_c	100 kPa s
Poisson's ratio of the cell ν_c	0.5
Cell layer thickness h_c	1 μm

Table 1: Globally fixed cell and substrate parameters.

with one of the three potential PA-stresses after optimization against the experimental data. One sees that the best combination is the Kelvin-Voigt model combined with the double sigmoid. The rectangular PA-profile would introduce discontinuous features in the strain energy response that are not present in the experiments. The exponential PA-profile would give an asymmetric response. Only the double sigmoid gives the smooth response observed experimentally. While the elastic model gives too steep curves, the Maxwell model needs different baselines before and after PA. The Kelvin-Voigt model gives near perfect fits.

8 Parametrization

In principle, one can minimize our theoretical predictions against our experimental readout (strain energy as a function of time) in regard to all model parameters. However, there are too many of them to get unique solutions and therefore we fix those parameters that are well established in the literature and only minimize for the ones that are specific to our experimental setup. Moreover the parameters of the substrate are known anyway. In Tab. 1, we list the fixed and known parameters. For the cell parameters, we use consensus values from the literature [1, 2, 6, 7]. In particular, cell stiffness is set to $E_c = 10 \text{ kPa}$, which is a typical value for strongly adherent cells. Setting cell viscosity to $\eta_c = 100 \text{ kPa} \cdot \text{s}$ corresponds to a viscoelastic relaxation time of $\tau = 10 \text{ s}$.

We next estimate the stiffnesses of substrate and adhesion layer. With $E_s = 4.47 \times 10^3 \text{ kPa}$, $h_s = 50 \mu\text{m}$ and $L_c \approx 50 \mu\text{m}$, we have for the substrate approximately $Y_s \approx 3 \times 10^8 \text{ N/m}^3$. For the effective spring constant of adhesions, a standard value is $k_a = 2.5 \text{ nN}/\mu\text{m} = 2.5 \text{ pN}/\text{nm}$ and a typical dimension is $d = 1 \mu\text{m}$. Thus we estimate $Y_a \approx k_a/\mu\text{m}^2 \approx 2 \times 10^9 \text{ N/m}^3$. This suggests that the adhesion layer is the stiffer element and that the cells perceive mainly the stiffness of the substrate.

The two parameters that are fitted to the baseline before PA are localization length l_p and background stress σ_{back} . These quantities represent the main characteristics of adhesion and force generation and together determine the substrate strain stored in the elastic substrate. Tab. 2 documents our results for the four different patterns used in the main text.

For the photoactivation part, we fit five parameters: the peak value for the double sigmoid σ_0 , and its

Fit parameter	Disc 500 µm	Disc 1000 µm	Disc 1500 µm	Hazard
Force localization length l_p	2.65 µm	3.75 µm	4.62 µm	2.97 µm
Contractile background stress σ_{back}	2.23 kPa	3.91 kPa	5.30 kPa	3.58 kPa

Table 2: Fit results for energy baseline.

Fit parameter	Disc 500 µm	Disc 1000 µm	Disc 1500 µm	Hazard
σ_0	1.2 kPa	1.8 kPa	1.8 kPa	0.8 kPa
σ_{max}	1.2 kPa	1.7 kPa	1.7 kPa	0.7 kPa
t_{act}	46 s	79 s	66 s	59 s
t_{rel}	291 s	416 s	343 s	335 s
τ_{act}	13 s	33 s	19 s	20 s
τ_{rel}	42 s	60 s	52 s	78 s

Table 3: Fit parameter for 100 ms PA-duration.

four time values. From this, one can calculate also the maximal stress σ_{max} achieved during PA. The corresponding results are given in Tab. 3. The results for the pulses are given in Tab. 4. The resulting strain energy curves and their interpretations are given in the main text.

9 Scaling considerations from analytical model

We now can use our analytical solution for the isotropic contractile disc in the limit of large disc size to rationalize our findings. We first note that a typical overall cell force is $F_{\text{tot}} = \mu N$. We therefore estimate for the background stress

$$\sigma_{\text{back}} = \frac{F_{\text{tot}}}{2\pi r_0 h_c} \approx 10 \text{ kPa} \quad (35)$$

in very good agreement with the order of magnitude of our fit results. We also note that the background stress sets the order of magnitude for cell elasticity, which we here fix to $E_c = 10 \text{ kPa}$.

For the localization length, we estimate

$$l_p = \left(\frac{E_c h_c}{Y(1 - \nu_c^2)} \right)^{1/2} \approx 1 \text{ } \mu\text{m} \quad (36)$$

again in very good agreement with the order of magnitude of our fit results.

Finally for the strain energy we estimate

$$U_s = \frac{\pi (\sigma_0 h_c)^2 r_0}{2 Y_s} \frac{r_0}{l_p} \approx 1 \text{ pJ} \quad (37)$$

again in very good agreement with the experimentally measured and fitted order of magnitude. Together, these estimates show that our theory is consistent and predictive.

PA duration	10 ms	20 ms	50 ms	100 ms	150 ms	200 ms
Fit parameter	Values					
Disc						
σ_0	0.6 kPa	1.1 kPa	1.5 kPa	1.7 kPa	1.9 kPa	1.9 kPa
σ_{\max}	0.6 kPa	1.1 kPa	1.4 kPa	1.6 kPa	1.9 kPa	1.8 kPa
t_{act}	72 s	71 s	89 s	105 s	96 s	105 s
t_{rel}	255 s	324 s	382 s	453 s	462 s	465 s
τ_{act}	10 s	21 s	30 s	33 s	49 s	48 s
τ_{rel}	34 s	35 s	48 s	53 s	39 s	67 s
Hazard						
σ_0	0.9 kPa	1.0 kPa	0.9 kPa	0.9 kPa	0.9 kPa	0.9 kPa
σ_{\max}	0.3 kPa	0.5 kPa	0.7 kPa	0.8 kPa	0.9 kPa	0.8 kPa
t_{act}	34 s	49 s	50 s	63 s	62 s	77 s
t_{rel}	130 s	186 s	267 s	278 s	350 s	275 s
τ_{act}	16 s	27 s	16 s	15 s	12 s	14 s
τ_{rel}	141 s	102 s	74 s	54 s	45 s	57 s

Table 4: Fit parameter for long opto protocol. Stresses rounded to one digit after comma.

10 Effect of actin organization on strain energy level in the model

Since in our model fits yield different l_p for hazard and disc pattern, respectively which influences the substrate strain energy $U_s \sim Y^2 \sim 1/l_p^4$ we choose a set of dummy parameters to purely study the influence of the adhesion geometry on the substrate strain energy. As in our example for the isotropic contractile disc we set $\sigma_{\text{back}} = 4 \text{ kPa}$ and $l_p = 4 \mu\text{m}$. This yields baseline strain energy values of $U_s^{\text{Hazard}} = 0.29 \text{ pJ}$ and $U_s^{\text{Disc}} = 0.24 \text{ pJ}$. Since all cell parameters are identical we conclude that the strain energy is strongly influenced by the internal stress fiber organization. The length of the “effective” boundary is given by $B^{\text{Hazard}} = (\frac{3}{2}\pi + 3)r_0$. Since U_s is essentially proportional to the length along which the traction acts (marked in red for the hazard) we can compute the ratio of B and the circumference of a circle, which is the effective boundary for the circle pattern, and compare it to the ratio of the two strain energy values listed above. The first ratio yields a value of $B^{\text{Hazard}}/(2\pi r_0) = 1.23$ while the ratio of the strain energy gives $U_s^{\text{Hazard}}/U_s^{\text{Disc}} = 1.21$ such that this very minimal consideration could explain the observed strain energy difference.

However, it is not possible to follow the same argumentation when it comes to strain energy response upon photo activation. Additionally, the model alone is not sufficient to explain this observation since model parameters were fitted such that they resemble the experimentally measured strain energy response. Very generally, the less effective force generation on the hazard pattern could be the result of either more stressed stress fibers which have less force generation capacity or simply the result of differing stress fiber densities within the two conditions. Regarding the very similar baseline stress

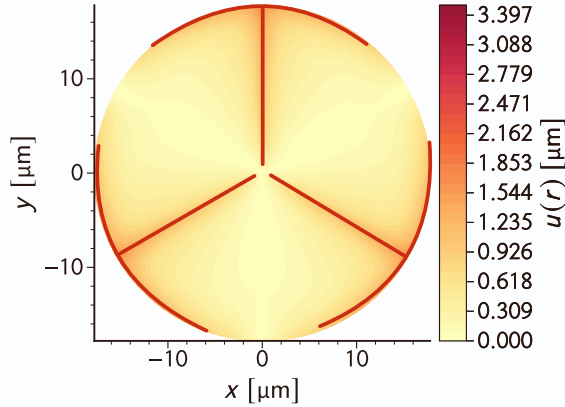


Figure 5

levels for hazard and disc those two explanations could be equivalent.

11 Example for python FEM-code for contractile disc

Our model was implemented in the FEM-framework FEniCS [9]. As an example of our code, here we document the calculation for the isotropic contractile disc.

```

1  from dolfin import *
2  import numpy as np
3  import sys
4  import logging
5  logging.basicConfig(level=logging.DEBUG)
6  logger = logging.getLogger("rothemain.rothe_utils")
7  logging.getLogger('UFL').setLevel(logging.WARNING)
8  logging.getLogger('FFC').setLevel(logging.WARNING)
9  set_log_active(False)
10 tol_x = DOLFIN_EPS
11 tol_y = DOLFIN_EPS
12 ''' Sample script for the Finite Element Simulation of an isotropic contractile disc with elastic
13     foundation.
14     Script was written for the 2019 version of FEniCS and run inside a Docker container build from the
15     2019 image quay.io/fenicsproject/stable:"version"
16
17     Copyright: Dennis Woerthmueller, Dimitri Probst
18     Last modification: August 29, 2021
19 '''
20
21 # Strain
22 def eps(v):
23     # Calculate the symmetric strain tensor.
24     return sym(grad(v))
25
26 # Stress
27 def sigma(v, lmbda, mu):
28     # Calculate the stress tensor based on constitutive relation for a linear elastic solid.
29     return 2.0 * mu * eps(v) + lmbda * tr(eps(v)) * Identity(len(v))
30
31 # Active stress tensor
32 def active(sx, sy, sxy=0.0):
33     # Define the tensor for the active stress contribution.
34     return as_tensor([[sx, sxy], [sxy, sy]])

```

```

32
33 # Calculation of the penetration length on a thick substrate
34 def penetrationLength_thick_subs(Ec, hc):
35     # Formulas taken from: Banerjee & Marchetti (2012): Contractile stresses in cohesive cell
36     # layers on finite-thickness substrates
37     ka = 2.5e-3          # Stiffness of focal adhesion bonds [N/m]
38     L = 50e-6            # Cell length (1d), diameter (2d) [m]
39     lc0 = 1e-6           # Length of sarcomeric subunit [m]
40     hs = 50e-6           # Thickness of the substrate [m]
41     nus = 0.5            # Poisson's ratio of the substrate
42     Es = 4.47e3          # Elastic modulus of the substrate [N/m^2]
43     heff = (1. / (hs * 2 * np.pi * (1 + nus)) + 1. / L)**-1
44     Ya = ka / (L * lc0)
45     Ys = (np.pi * Es) / heff
46     Y = (1.0 / Ya + 1.0 / Ys)**(-1)
47     #print Ya, Ys
48     lp = np.sqrt(Ec * hc / Y)
49     return lp, Ys / 1e12
50
51 # only relevant if symmetry if pattern is present and if PA is on full cell
52 def DirichletBoundary(x, on_boundary):
53     # Define the dirichlet boundary condition for center of the circular cell.
54     return near(x[0], 0.0, tol_x) and near(x[1], 0.0, tol_y)
55
56 # strain energy
57 def calculateStrainEnergy(u, kN, Ys, F, V, assigner_V_to_F, mesh):
58     # calculate strain energy of the cell according to formula defined in the theory supplement.
59     ux = Function(F)
60     uy = Function(F)
61     u0 = Function(V)
62     u0.assign(u)
63     u0.vector()[:] *= u0.vector()
64     # Split so that ux = ux**2, uy = uy**2
65     assigner_V_to_F.assign([ux, uy], u0)
66     # ux will hold |u|**2 = ux**2 + 1 * uy**2
67     ux.vector().axpy(1, uy.vector())
68     return assemble(0.5*kN**2/Ys*ux*dx(mesh))
69
70 # function which defines the simulation
71 def isotropic_contractile_disc():
72
73     # Import a pre-created mesh (e.g. with gmsh)
74     mesh = Mesh('circ_1000.xml')
75
76     # set fixed cell parameters
77     E3D = 10e3 # Elastic modulus of the cell in Pa
78     eta3D = 100e3 # Viscous modulus of the cell Pa*s
79     h = 1e-6 # cell height in m
80     sigma_back2D = 4e-03 # 2D stress N/m, conversion between 2D and 2D via sigma_2D = sigma_3D*h
81     sigma0 = 5e-03 # 2D active stress in N/m
82
83     # conversion to 2D constants for plane stress and thin layer approximation
84     Eh = E3D * h # N / m = Pa * m
85     etah = eta3D * h # Ns / m = Pa * m
86     nu = 0.5
87     lmbdaE = Eh * nu / ((1 - nu) * (1 + nu)) # in 3D given by: ((1 + nu) * (1 - 2 * nu))
88     muE = Eh / (2 * (1 + nu))
89     lmbdaEta = etah * nu / ((1 - nu) * (1 + nu)) # in 3D given by: ((1 + nu) * (1 - 2 * nu))
90     muEta = etah / (2 * (1 + nu))
91     _, Ys = penetrationLength_thick_subs(E3D, h) # Unit [m]. Here, only Ys is calculated!
92     lp = 4*1e-6 # force penetration length in m; in our approach a fit parameter of strain energy
93     # baseline fit
94     kN = Constant((lmbdaE + 2 * muE) / (lp * 1e6)**2) # Spring stiffness density kN in N / m / um**2
95     # to get u (displacement field) in um
96
97     # Define Time Stepping

```

```

96 dt = Constant(15) # Time constant in s, definde in UFL (unified form language)
97 T = 1005 # Total simulation time in s, make sure that T mod dt= 0 otherwise last time step is
98 missing
99 lag_time = 3 * etah / Eh # Natural time scale of the system which describes the time the cell
100 needs to arrive in its 'ground state'.
101 act_times = np.array([300,T+15]) + lag_time # Time points of photo activation stress
102
103 # Define function space and basis functions
104 V = VectorFunctionSpace(mesh, "CG", 2) # continuous Galerkin of degree 2 (Lagrange polynomials)
105 u = TrialFunction(V)
106 v = TestFunction(V)
107
108 # Define boundary condition
109 u0 = Constant((0.0, 0.0)) # zero displacement in symmetry center of the disc
110 bc = DirichletBC(V, u0, DirichletBoundary)
111
112 # Define variational form in Dolfin UFL syntax with a backward euler time discretization scheme
113 a = inner(sigma(u, lmbdaEta, muEta), sym(grad(v)))*dx + dt*inner(sigma(u, lmbdaE, muE), sym(grad(v
114 )))*dx + dt * kN * inner(u, v) * dx
115 u = Function(V)
116 uinit = Constant((0.0, 0.0))
117 uold = interpolate(uinit, V)
118 uold.assign(u)
119
120 # Define Elements and Function Space for resulting Tensors
121 F = FunctionSpace(mesh, 'CG', 2)
122 assigner_V_to_F = FunctionAssigner([F, F], V)
123 dFE = FiniteElement("DG", mesh.ufl_cell(), 0)
124 tFE = TensorElement(dFE)
125 W = FunctionSpace(mesh, tFE)
126 K = FunctionSpace(mesh, dFE)
127 stress = Function(W, name='Stress')
128 disp = Function(V, name='Displacement')
129
130 # Determine the save options and save resulting fields to output.xdmf to view with ParaView
131 xdmf_file= XDMFFile("simulation_result.xdmf")
132 xdmf_file.parameters["flush_output"] = True
133 xdmf_file.parameters["functions_share_mesh"] = True
134 save = True
135
136 # Initialize lists to save simulation results
137 all_times = []
138 all_energies = []
139
140 # Run simulation
141 t = 0 * dt # start time
142 lag_counter = 0 # counts the number of time needed for lag time
143 act_flag = False # True, if activated
144 sigma_act = 0.0 # initial photo activation stress
145
146 # in the example we use an exponential shaped activation profile with the following free time
147 # parameters:
148 tau_stress_act = 30 # time scale for activation
149 act_duration = 300 # duration photo activation
150 tau_stress_rel = 40 # time scale for relaxation
151
152 # main simulation loop, time evolution. Solve system for each time step.
153 while t(0.0) <= T + lag_time:
154     print(t(0.0))
155     if t(0.0) < lag_time: # count the number of time steps necessary for lag time
156         lag_counter += 1
157     if near(t(0.0), act_times[0]) and act_flag == False: # set act_flag to true if first
158         activation time point is reached
159         print("GOT ACTIVATED")
160         act_flag = True

```

```

156     if act_flag == True: # calculate the active stress contribution which is != 0
157         act_time = act_times[0]
158         newT = t(0.0) - act_time # times in activation function are measure relative to activation
159         time point
160         if newT <= act_duration: # acitvation
161             sigma_act = sigma0 * (1 - np.exp(-newT/ tau_stress_act))
162         else: # relaxation
163             sigma_act = sigma0 * (1 - np.exp(-act_duration / tau_stress_act)) * np.exp(-(newT-
164             act_duration)/tau_stress_rel)
165             if sigma_act < 1e-08:
166                 sigma_act = 0.0
167
168             # Right side of variational form
169             L = inner(sigma(uold, lmbdaEta, muEta), sym(grad(v))) * dx - \
170                 dt * inner(active(sigma_back2D+sigma_act, sigma_back2D+sigma_act), sym(grad(v))) * dx
171
172             # Solve problem with boundary conditions bc
173             solve(a == L, u, bc)
174             uold.assign(u) # assign solution to uold to use in next iteration time step
175             total_energy = calculateStrainEnergy(u, kN, Ys, F, V, assigner_V_to_F, mesh) # Unit pJ
176
177             # store data
178             all_times.append(t(0.0))
179             all_energies.append(total_energy)
180
181             # calculate total stress/strain tensors
182             eps = sym(grad(u))
183             sig = active(sigma_back2D+sigma_act, sigma_back2D+sigma_act) + Eh/(1+nu)*eps + nu*Eh/(1-nu**2)
184             *tr(eps)*Identity(2)
185             stress.assign(project(sig, W))
186             disp.assign(u)
187
188             # save tensors at each time step to xdmf-file
189             if save:
190                 xdmf_file.write(disp, t(0.0))
191                 xdmf_file.write(stress, t(0.0))
192             # update time step
193             t += dt
194
195             return None
196 # Main function
197 if __name__ == "__main__":
198     isotropic_contractile_disc() # simulate the photo activated isotropic contractile disc

```

References

- [1] C.M. Edwards and U.S. Schwarz. Force localization in contracting cell layers. *Physical Review Letters*, 107(12):128101, 2011.
- [2] S. Banerjee and M.C. Marchetti. Contractile stresses in cohesive cell layers on finite-thickness substrates. *Physical Review Letters*, 109(10):108101, 2012.
- [3] Aaron F Mertz, Shiladitya Banerjee, Yonglu Che, Guy K German, Ye Xu, Callen Hyland, M Cristina Marchetti, Valerie Horsley, Eric R Dufresne, et al. Scaling of traction forces with the size of cohesive cell colonies. *Physical Review Letters*, 108(19):198101, 2012.

- [4] Shiladitya Banerjee and M Cristina Marchetti. Controlling cell–matrix traction forces by extracellular geometry. *New Journal of Physics*, 15(3):035015, 2013.
- [5] P.W. Oakes, S. Banerjee, M.C. Marchetti, and M.L. Gardel. Geometry regulates traction stresses in adherent cells. *Biophysical Journal*, 107(4):825–833, 2014.
- [6] Medhavi Vishwakarma, Jacopo Di Russo, Dimitri Probst, Ulrich S Schwarz, Tamal Das, and Joachim P Spatz. Mechanical interactions among followers determine the emergence of leaders in migrating epithelial cell collectives. *Nature Communications*, 9(1):1–12, 2018.
- [7] Jana Hanke, Dimitri Probst, Assaf Zemel, Ulrich S Schwarz, and Sarah Köster. Dynamics of force generation by spreading platelets. *Soft Matter*, 14(31):6571–6581, 2018.
- [8] Josephine Solowiej-Wedderburn and Carina M Dunlop. Sticking around: Cell adhesion patterning for energy minimization and substrate mechanosensing. *Biophysical Journal*, 121(9):1777–1786, 2022.
- [9] M.S. Alnaes, J. Blechta, J. Hake, J. Johansson, B. Kehlet, A. Logg, C. Richardson, J. Ring, M.E. Rognes, and G.N. Wells. The FEniCS project version 1.5. *Archive of Numerical Software*, 3(100):9–23, 2015.
- [10] Patrick W Oakes, Elizabeth Wagner, Christoph A Brand, Dimitri Probst, Marco Linke, Ulrich S Schwarz, Michael Glotzer, and Margaret L Gardel. Optogenetic control of rhoa reveals zyxin-mediated elasticity of stress fibres. *Nature Communications*, 8:15817, 2017.